Neurobiology of Disease

CSMD3 Deficiency Leads to Motor Impairments and Autism-Like Behaviors via Dysfunction of Cerebellar Purkinje Cells in Mice

Ke Xi,[1,2,3*] Si-Qing Cai,[1,2,3*] Hui-Fang Yan,[6] Yue Tian,[1,2,3] Jie Cai,[1,2,3] Xiao-Mei Yang,[5] Jing-Min Wang,[6] and Guo-Gang Xing[1,2,3,4]

[1]Neuroscience Research Institute, Peking University, Beijing 100191, People's Republic of China, [2]Department of Neurobiology, School of Basic Medical Sciences, Peking University, Beijing 100191, People's Republic of China, [3]Health Science Center, Key Laboratory for Neuroscience, Ministry of Education of China and National Health Commission of China, Beijing 100191, People's Republic of China, [4]Second Affiliated Hospital of Xinxiang Medical University, Henan 453002, People's Republic of China, [5]Department of Human Anatomy and Embryology, School of Basic Medical Sciences, Peking University, Beijing 100191, People's Republic of China, and [6]Department of Pediatrics, Peking University First Hospital, Beijing 100034, People's Republic of China

Autism spectrum disorder (ASD) is a neurodevelopmental disorder with highly heritable heterogeneity. Mutations of CUB and sushi multiple domains 3 (*CSMD3*) gene have been reported in individuals with ASD. However, the underlying mechanisms of CSMD3 for the onset of ASD remain unexplored. Here, using male *CSMD3* knock-out ($CSMD3^{-/-}$) mice, we found that genetic deletion of *CSMD3* produced core autistic-like symptoms (social interaction deficits, restricted interests, and repetitive and stereotyped behaviors) and motor dysfunction in mice, indicating that the *CSMD3* gene can be considered as a candidate for ASD. Moreover, we discovered that the ablation of *CSMD3* in mice led to abnormal cerebellar Purkinje cell (PC) morphology in Crus I/II lobules, including aberrant developmental dendritogenesis and spinogenesis of PCs. Furthermore, combining *in vivo* fiber photometry calcium imaging and *ex vivo* electrophysiological recordings, we showed that the $CSMD3^{-/-}$ mice exhibited an increased neuronal activity (calcium fluorescence signals) in PCs of Crus I/II lobules in response to movement activity, as well as an enhanced intrinsic excitability of PCs and an increase of excitatory rather than inhibitory synaptic input to the PCs, and an impaired long-term depression at the parallel fiber–PC synapse. These results suggest that CSMD3 plays an important role in the development of cerebellar PCs. Loss of CSMD3 causes abnormal PC morphology and dysfunction in the cerebellum, which may underlie the pathogenesis of motor deficits and core autistic-like symptoms in $CSMD3^{-/-}$ mice. Our findings provide novel insight into the pathophysiological mechanisms by which *CSMD3* mutations cause impairments in cerebellar function that may contribute to ASD.

Key words: **autism spectrum disorder; cerebellar Purkinje cells; CUB and Sushi Multiple Domains 3; long-term depression; motor impairments; synaptic plasticity**

Significance Statement

Autism spectrum disorder (ASD) is a neurodevelopmental disorder with highly heritable heterogeneity. Advances in genomic analysis have contributed to numerous candidate genes for the risk of ASD. Recently, a novel giant gene *CSMD3* encoding a protein with CUB and sushi multiple domains (CSMDs) has been identified as a candidate gene for ASD. However, the underlying mechanisms of *CSMD3* for the onset of ASD remain largely unknown. Here, we unravel that loss of *CSMD3* results in abnormal morphology, increased intrinsic excitabilities, and impaired synaptic plasticity in cerebellar PCs, subsequently leading to motor deficits and ASD-like behaviors in mice. These results provide novel insight into the pathophysiological mechanisms by which *CSMD3* mutations cause impairments in cerebellar function that may contribute to ASD.

Received Sep. 27, 2022; revised Mar. 18, 2023; accepted Apr. 5, 2023.

Author contributions: K.X. and G.-G.X. designed research; K.X., S.-Q.C., and H.-F.Y. performed research; K.X., S.-Q.C., H.-F.Y., Y.T., J.C., X.-M.Y., J.-M.W., and G.-G.X. contributed unpublished reagents/analytic tools; K.X., S.-Q.C., H.-F.Y., Y.T., J.C., X.-M.Y., and G.-G.X. analyzed data; K.X. and G.X. wrote the paper.

This work was supported by the National Key R&D Program of China (Grant 2019YFC1712104), the National Natural Science Foundation of China (Grants 82171226, 81974169, and 81671085), the Natural Science Foundation of Beijing Municipality (Grant 7222105), and King's College London–Peking University Health Science Center Joint Institute for Medical Research Program (Grant BMU2021KCL001). We thank the animal caretakers for their services at the Department of Laboratory Animal Science, Peking University Health Science Center.

*K.X. and S.-Q.C. contributed equally to this work.

The authors declare no competing financial interests.

Correspondence should be addressed to Guo-Gang Xing at ggxing@bjmu.edu.cn or Jing-Min Wang at wang66jm@163.com or Xiao-Mei Yang at xiaomeiyang@bjmu.edu.cn.

https://doi.org/10.1523/JNEUROSCI.1835-22.2023

Introduction

Autism spectrum disorder (ASD) is a highly heritable, clinically and genetically heterogenous neurodevelopmental disorder characterized by deficits in social communication and interaction along with the presence of restricted interests and repetitive behaviors (Lord et al., 2018). Advances in genomic analysis have contributed to numerous candidate genes for the risk of ASD, and these genes are involved in various biological processes, including dendritic growth, axonogenesis, and synapses formation (Havdahl et al., 2021). Recently, a novel giant gene *CSMD3* encoding a protein with CUB and Sushi multiple domains (CSMD) has been identified as a candidate gene for ASD (Shimizu et al., 2003; Floris et al., 2008). *CSMD3* is a giant gene of 1.2 Mb consisting of 73 exons, encodes a large transmembrane protein of CSMD3, and is expressed mainly in fetal and adult brains (Shimizu et al., 2003). CSMD3 protein belongs to the CSMD family, which also includes CSMD1 and CSMD2 (Lau and Scholnick, 2003). All three CSMD family proteins have 14 CUB domains and 26–28 Sushi domains (Lau and Scholnick, 2003; Shimizu et al., 2003), and these CUB and Sushi domain-containing proteins generally mediate protein–protein interactions between extracellular and transmembrane proteins (Gaboriaud et al., 2011), and are known to regulate neuronal migration, dendrite growth, and synapse formation (Gunnersen et al., 2007; Chen et al., 2008; Sia et al., 2013), suggesting a role of CSMD3 in neuronal development and maturation. CSMD3 may act as a coreceptor for unknown extracellular or transmembrane proteins via its CUB and Sushi domains, to regulate dendrite development in cultured hippocampal neurons (Mizukami et al., 2016). Therefore, malfunctions of CSMD3 may be one of the factors in the pathogenesis of some neurodevelopmental disorders, such as epilepsy, schizophrenia, and autism. In fact, the *CSMD3* gene is identified as a candidate gene for benign adult familial myoclonic epilepsy (Shimizu et al., 2003), and mutations of the *CSMD3* gene were found in some autism and schizophrenia patients (Floris et al., 2008; Malhotra et al., 2011), indicating that deficiencies in CSMD3 protein are involved in the onset and progression of these disorders.

Emerging data have implicated dysfunction of the cerebellum in ASD pathogenesis (Hampson and Blatt, 2015; Su et al., 2021), with postmortem studies in ASD patients showing cerebellar Purkinje cell (PC) loss (Bauman and Kemper, 2005; Amaral et al., 2008), and isolated cerebellar injury has been associated with a higher incidence of ASD (Limperopoulos et al., 2007). In addition, structural abnormalities (Skefos et al., 2014; Stoodley, 2014), functional deficits or abnormal development (Oristaglio et al., 2013; van der Heijden et al., 2021), and diminished or abnormal cerebrocerebellar connectivity (Hanaie et al., 2018; Oldehinkel et al., 2019; Ramos et al., 2019), have been detected in the cerebellums of individuals with ASD. Studies with mouse models of ASD have also shown that dysfunction of PCs in the cerebellum is sufficient to confer ASD-like behaviors (Tsai et al., 2012; Peter et al., 2016; Stoodley et al., 2017). Moreover, ASD patients often manifest deficits in motor coordination and delayed development of motor skills that are associated with cerebellar function (Harris, 2017; Wilson et al., 2018), and the cerebellum is among the most prominent brain regions demonstrating high coexpression of ASD-associated genes (Menashe et al., 2013). Selective deletion of *Tsc1*, *Pten*, or *Shank2* gene in cerebellar PCs replicates autism-resembling social behavior deficits in mice (Tsai et al., 2012; Cupolillo et al., 2016; Peter et al., 2016). However, the potential roles of CSMD3 in the regulation of functioning of cerebellar PCs and associated behavioral phenotypes have remained unknown.

Here, using male *CSMD3* deletion ($CSMD3^{-/-}$) mice, we demonstrate for the first time, to our knowledge, that loss of CSMD3 results in abnormal morphology, increased intrinsic excitabilities, and impaired synaptic plasticity in cerebellar PCs of Crus I/II lobules, subsequently leading to motor deficits and ASD-like behaviors in mice. These results provide novel insight into the pathophysiological mechanisms by which *CSMD3* mutations cause impairments in cerebellar function that may contribute to ASD.

Materials and Methods

Chemicals, reagents, and antibodies

For electrophysiological recording, chemicals including pentobarbital sodium (P3761), ATP magnesium salt (MgATP; catalog #A9187), GTP sodium salt hydrate (Na_3GTP; catalog #G8877), potassium D-gluconate (K-gluconate; catalog #G4500), cesium methanesulfonate (CsMeS; catalog #C1426), cesium chloride (CsCl; catalog #C4036), and EGTA (catalog #324626) were purchased from Sigma-Aldrich. Alexa Fluor 546-conjugated streptavidin (catalog #S11225) and biocytin (catalog #HY-101884), respectively, were purchased from Thermo Fisher Scientific and MedChemExpress. D(−)-2-amino-5-phosphonopentanoic acid (D-AP5; catalog #0106) and picrotoxin (PTX; catalog #1128) were obtained from Tocris Bioscience. Tetraethylammonium chloride (TEACl; catalog #sc-202834) was purchased from Santa Cruz Biotechnology; QX-314 bromide (catalog #ab120117) was purchased from Abcam; and NBQX disodium salt (catalog #T4113) was purchased form TargetMol. For cell culture experiments, the human oligodendrocyte MO3.13 cell line was obtained from CELLutions Biosystems. DMEM (catalog #11965092), B27 (catalog #17504044), GlutaMAX (catalog #35050061), and L-glutamine (catalog #A2916801) were purchased from Thermo Fisher Scientific. Fetal bovine serum (FBS; catalog #SPC900A) was purchased from ScienProCell. Poly-D-lysine (catalog #P6407) and phorbol 12-myristate 13-acetate (PMA; catalog #P8139) were purchased from Sigma-Aldrich. For immunofluorescent staining, primary antibodies including mouse anti-calbindin (CB; catalog #C9848), mouse anti-myelin basic protein (MBP; catalog #AMAB91062), and mouse anti-neuronal-specific nuclear protein (NeuN; catalog #C87804) were purchased from Sigma-Aldrich. Rabbit anti-CSMD3 (catalog #orb2197) was obtained from Biorbyt. Mouse anti-parvalbumin (PV; catalog #MAB1572) and mouse anti-GFAP (catalog #3670) were purchased from Cell Signaling Technology. Mouse anti-calretinin (CR; catalog #6B3) was purchased from Swant. Goat anti-Iba1 (catalog #011–27991) was obtained from FUJIFILM. All secondary antibodies, including Alexa Fluor 488 donkey anti-mouse IgG (catalog #715–545-150), Cyanine Cy3 donkey anti-mouse IgG (catalog #715–165-150), and Alexa Fluor 488 donkey anti-rabbit (catalog #711–545-152) were purchased from Jackson ImmunoResearch. DAPI (catalog #C0060) was purchased from Solarbio. For immunohistochemical staining and Golgi–Cox staining, a SP Kit (catalog #SP-9001), DAB Horseradish Peroxidase Color Development Kit (catalog #P0203), and Hito Golgi–Cox Optimstain kit (catalog #HTKNS1125) were purchased from ZSGB-BIO, Beyotime, and Hitobiotec, respectively. For calcium recording, adeno-associated virus (AAV) vectors containing a Cre-dependent virus rAAV2/9-EF1α-DIO-GCaMP6s (catalog #PT-0071), rAAV2/9-VGAT1-Cre (catalog #PT-0346), and rAAV2/9-L7-GCaMP6s (catalog #PT-3318) were purchased from Brain-VTA. For sparse labeling, AAV vectors containing a Cre-dependent virus rAAV-L7-cre (catalog #PT-0568) and rAAV-EF1α-DIO-EYFP (catalog #PT-0012) were purchased from Brain-VTA. Unless otherwise specified, all other chemicals and reagents were purchased from Sigma-Aldrich.

Animals

The genetic background of all mice is C57BL/6J. The mice were housed and bred under specific pathogen-free conditions at the Health Science Center, Peking University. All animal experiments were performed in accordance with the guidelines of the National Institutes of Health *Guide for the Care and Use of Laboratory Animals* and were approved by the Ethics Committee of Peking University Health Science Center. All

data derived from animal studies were analyzed by an experimenter blind to experimental conditions. The order of the animals was further randomized before behavioral tests. Only male animals were used for all experiments.

CSMD3$^{-/-}$ mice were generated on a C57BL/6J background by CRISPR/Cas9-mediated gene targeting in the Shanghai Model Organisms Center, as illustrated in Figure 1. Briefly, we designed target guide RNA specific to exon 2 of a main spliceosome (*CSMD3*-201), which was microinjected into the fertilized eggs of C57BL/6J mice. Integration of the targeting construct was confirmed by Southern blot. Targeted embryonic stem cell lines were injected into C57BL/6J blastocysts. Genomic DNA was extracted from tail biopsies for PCR genotyping and sequencing. To amplify the *CSMD3* mutant allele (450 bp) and the wild-type (WT) allele (450 bp), *CSMD3* mutant and wild-type alleles were detected by PCR with the following primers: *CSMD3* knock-out cassette, forward (F): 5′-CTATGAACATATGCACAATTCCTACTG-3′; and reverse (R): 5′-ATGAGCAGACAAAACAGTCAGAGTG-3′; and *CSMD3* deleted exon region, F: 5′-TGTCCAAGTGCTAATCCT GGTAAA-3′; and R: 5′-ATGAGCAGACAAAACAGTCAGAGTG-3′.

Reverse transcription PCR and quantitative real-time PCR

Total RNA was extracted and purified from fresh mouse tissues using TRIzol Reagent (Thermo Fisher Scientific), and reverse transcription to cDNA was performed with oligo deoxythymidine primers and Moloney murine leukemia virus reverse transcriptase (Promega) according to the manufacturer protocol. Template cDNA (1 μl) was amplified by PCR with Taq DNA polymerase (Takara) in 25 μl total reaction volume containing 0.5 μM PCR primer as indicated. Quantitative real-time PCR (qRT-PCR) was performed on the ABI 7500 Fast real-time PCR system (Thermo Fisher Scientific) with SYBR Premix Ex Taq II (Takara). The PCR program consisted of 95°C for 5 min; 40 cycles of 95°C for 10 s, 63°C for 30 s, and 72°C for 30 s; and 72°C for 5 min. β-Actin was used as an internal control. The relative expression of mRNA level was quantified via the $2^{-\Delta\Delta CT}$ method as described previously (Fang et al., 2015). The F and R primers used for amplification were as follows: F: 5′-CGGAATGGTGACGGACGAGAAC-3′; and R: 5-GCCTCCACA AGGTGCTATACAGAC-3′.

Cell culture

Human oligodendrocyte MO3.13 cells (CELLutions Biosystems) were revived as per the manufacturer instructions and maintained in complete growth medium consisting of DMEM supplemented with 2 mM L-glutamine, 1% penicillin/streptomycin (P/S), and 10% FBS, in a humidified incubator with an atmosphere of 5% CO_2, at 37°C. Cells were seed on glass coverslips (at 2.5×10^4 cells/cm^2) into 24-well plates and maintained 24 h for plating. Then, the medium was replaced by differentiation medium (DM), consisting of serum-free DMEM, supplemented with 2 mM L-glutamine, 1% P/S, and 10 nM PMA. Cells were cultured in DM for 5 d, after which time they were used in experiments.

Primary cultured hippocampal neurons were prepared from embryonic day 17 C57BL/6J mice as described previously (Zhao et al., 2017). Cells were seeded onto coverslips coated with poly-D-lysine (1 mg/ml; Sigma-Aldrich) at a density of 100,000/coverslip. Neurons were cultured in Neurobasal Medium supplemented with 2% Gibco B27 (Thermo Fisher Scientific), 1% GlutaMAX (Thermo Fisher Scientific) at 37°C in a humidified atmosphere of 5% CO_2. Thereafter, half of the culture medium was replaced by the fresh medium every 72 h.

Immunofluorescent staining

For immunostaining of CSMD3 with MBP in cultured MO3.13 cells, or with NeuN in cultured hippocampal neurons, cultured medium was removed, and cells (plated on coverslips) were fixed in 2% paraformaldehyde (PFA) in sodium PBS for 30 min, permeabilized with 0.1% Triton X-100, and blocked with 5% donkey serum for 40 min. Then, the cells were incubated with the primary antibodies, including rabbit anti-CSMD3 (1:300), mouse anti-MBP (1:500), and mouse anti-NeuN (1:200) overnight at 4°C. After three washes in PBS, samples were incubated with appropriate secondary antibodies, including Alexa Fluor 488 donkey anti-rabbit (1:1000) and donkey polyclonal anti-mouse Cy3 (1:1000) at room temperature for 1 h. The cells were counterstained with the nuclear marker DAPI (100 ng/ml) carrying blue fluorescence for 10 min at room temperature. After three washes with PBS, coverslips were mounted on microscope slides and imaged. Negative controls were obtained by repeating the above procedure with the omission of the CSMD3 antibody.

For immunostaining of CSMD3 with calbindin in cerebellar tissues, deeply anesthetized mice were intracardially perfused with 30 ml of 0.1 M phosphate buffer (PB) at pH 7.4, followed by 50 ml of cold 4% PFA (in 0.1 M PB). After perfusion, the brains were removed quickly, postfixed for 8 h in the perfusion fixative, and cryoprotected in 30% sucrose (in 0.1 M PBS) overnight at 4°C. Sagittal 30-μm-thick serial sections of the cerebellum were cut with a freezing microtome (model CM1950, Leica). The sections were washed three times in PBS for 5 min each and blocked with 5% donkey serum for 1 h at room temperature. Then, the sections were incubated with the primary antibodies, including mouse anti-calbindin (1:500), mouse anti-NeuN (1:500), mouse anti-PV (1:400), mouse anti-CR (1:750), mouse anti-MBP (1:500), mouse anti-GFAP (1:600), goat anti-Iba1 (1:800), and rabbit anti-CSMD3 (1:300), overnight at 4°C. After washing three times in PBS, the sections were incubated with the secondary antibodies, including Alexa Fluor 488 donkey anti-mouse IgG (1:1000), cyanine Cy3 donkey anti-mouse IgG (1:1000), and Alexa Fluor 488 donkey anti-rabbit IgG (1:1000) at room temperature for 2 h. Sections were counterstained with the nuclear marker DAPI (100 ng/ml) carrying blue fluorescence for 10 min at room temperature. Visualization of fluorescence signal was performed by confocal microscopy at excitation wavelengths of 488 nm (green), 543 nm (red), and 405 nm (blue). At least four fields per section were analyzed to establish reproducibility.

Golgi–Cox staining

Staining was performed on freshly dissected tissue obtained from pentobarbital sodium-anesthetized mice using a Golgi–Cox Optimstain Kit (catalog #HTKNS1125, Hito). The cerebellum was dissected immediately after mice were killed and tissue was impregnated in the mix of solution 1 and 2 for 2 weeks in the dark. The tissue was then transferred into solution 3 at least five times the volume of the tissue and was stored at 4°C in the dark for 72 h. The tissues were then sectioned sagittally into 150 μm sections on a vibratome, and the sections were mounted on gelatin-coated slides. Mounting slides were dried at a 37°C oven overnight and were ready for the following staining: 3 min in distilled water twice, 10 min in staining solution, 4 min in distilled water twice. Next, slides were dehydrated in a graded series of ethanol (5 min in 50%, 5 min in 70%, 5 min in 95%, and 5 min in 100% ethanol three times) and cleared in xylene two times, for 5 min each. The slides were then coverslipped with permount and stored in the dark until morphologic analysis was performed. Images were processed and spine density quantified using ImageJ software (National Institutes of Health) with studies performed by examiner blinded to genotypes. The spine density was expressed as the number of spines per 1 μm dendrite.

Behavioral studies

All behavioral experiments were conducted blind with the treatment and genotype of the mice; that is, the behavioral experimenters were kept blind from the groupings of the mice.

Three-chamber sociability test. Three-chamber sociability test was performed as previously described (Peça et al., 2011) with minor modifications. Briefly, the customized social test apparatus consisted of the following three chambers: a middle chamber (10 × 20 cm) and another two chambers (20 × 20 cm). Before the social approach test, target subjects (Stranger 1 and Stranger 2) were 5- to 6-week-old male mice habituated to being placed inside perforated acrylic cages (11 × 11 × 11 cm) for 3 d. Test mice were habituated to the testing room for at least 45 min before the start of behavioral test. Then, the test mouse was placed in the center chamber for 10 min habituation, after which it was allowed to freely explore all three chambers for 10 min. After this, a subject mouse of Stranger 1 (S1) was placed in one of the side chambers and an objective (O) was placed in the other side. The test mouse was then allowed to

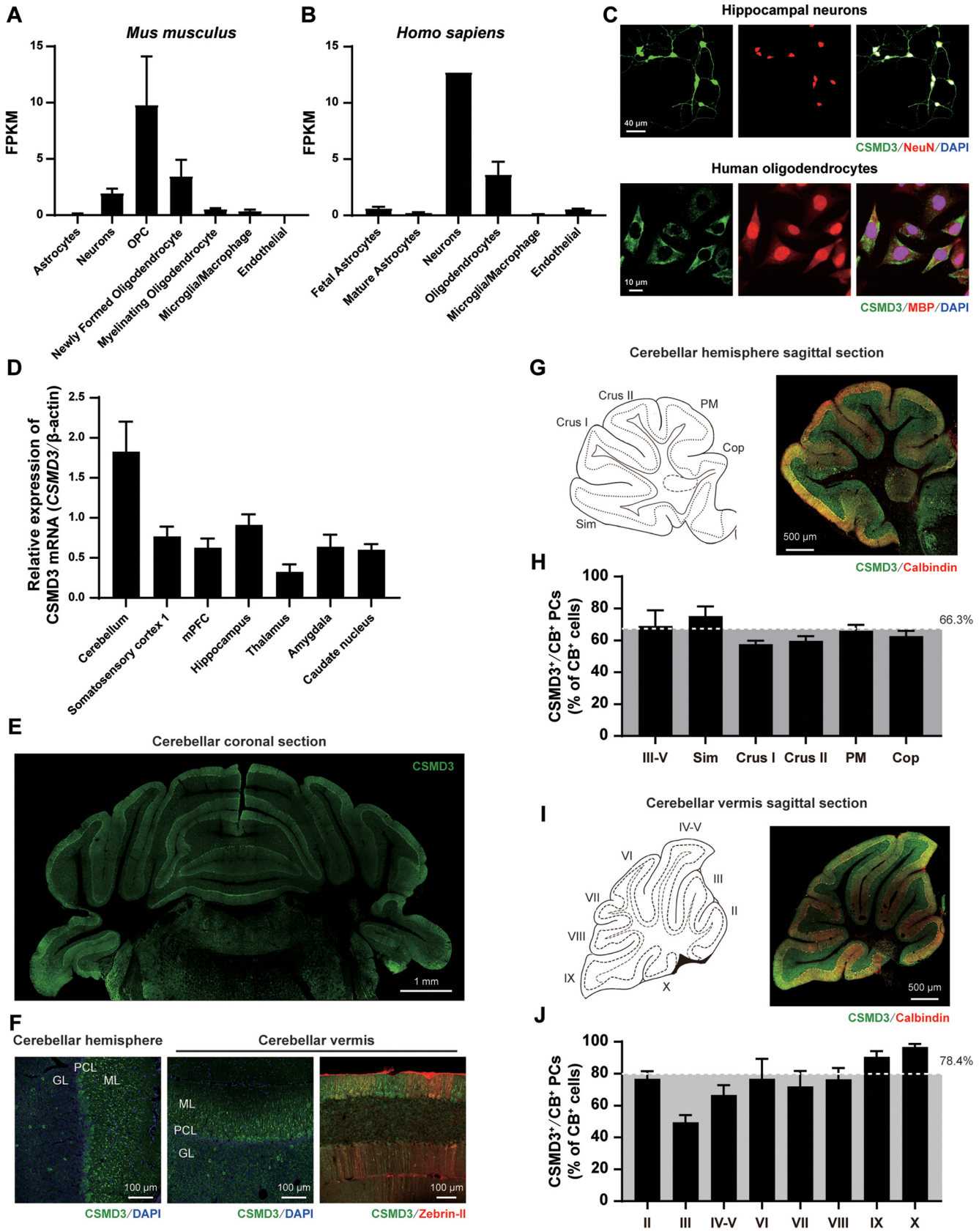

Figure 1. Distribution of CSMD3-expressing cells in the cerebellar cortex. ***A***, ***B***, Brain RNA-Seq database analysis of CSMD3 mRNA expression in different cell types: from Mus musculus (***A***); from Homo sapiens (***B***). FPKM, Fragments per kilobase of transcript per million mapped. ***C***, Immunofluorescence staining of CSMD3 (green) with NeuN, MBP (red), and DAPI (blue) in cultured hippocampal neurons (top) and MO3.13 human oligodendrocyte cells, respectively. Scale bars: top, 40 μm; bottom, 10 μm. ***D***, qRT-PCR analysis of CSMD3 mRNA expression in the brains of adult mice. ***E***, Immunostaining of CSMD3 (green) in cerebellar coronal section of adult wild-type mice. Scale bar, 1 mm. ***F***, Representative high-magnification images of CSMD3 immunostaining in cerebellar hemisphere (left) and vermis (middle and right), respectively. Note that the CSMD3-expressing cells are present in the PCL, as well as in the ML and GL in both hemisphere (left)

explore for 10 min. Then, the objective was replaced with Stranger 2 (S2), and the test mouse was allowed to explore for an extra 10 min. The time the test mouse spent in each chamber was recorded and analyzed (Smart 3.0, Panlab).

Grooming behaviors. Grooming behaviors were measured as described previously (Guo et al., 2019). In brief, male mice (age, 5–6 weeks) were placed individually in a clean cage with a thin layer of fresh bedding. After 1 h's habituation to the cage, the grooming behaviors of mice were video recorded in the dark for 30 min. The measured grooming behaviors included face wiping, scratching/rubbing of head and ears, and full-body grooming. After recording the behaviors, the experimenters were blinded to the genotypes and manually analyzed the videotapes. The average of 30 min of grooming time was calculated, and grooming times per 10 min were presented.

Marble-burying test. The marble-burying test was performed as previously reported (Wang et al., 2018). Briefly, fresh, unscented mouse bedding material was added to each standard polycarbonate mouse cage to a depth of 5 cm to level the bedding surface. Standard glass marbles were placed gently on the surface of the bedding in four rows of two marbles. Mice were transported to the testing room for acclimation 1 h before testing, then placed into the prepared testing cages and left undisturbed for 1 h. Only marbles under one-third of the bedding in depth were marked as buried marbles.

Spontaneous digging behavior. Male mice (age, 5–6 weeks) were placed individually in a clean cage with fresh bedding tamped down to a depth of ~5 cm. After 1 h of habituation to the cage, the spontaneous digging behavior of mice was video recorded in the dark for 10 min. Each mouse was tested individually using fresh bedding. After recording, the experimenters were blinded to the genotypes and manually analyzed the videotapes.

New object recognition test. The new object recognition (NOR) test was performed as previously reported (Chao et al., 2020; Cruz-Sanchez et al., 2020; Shimoda et al., 2021). All mice were subjected to habituation in the black context without any spatial cue for 1 h in the first 3 d, and exposed to the open field for 10 min on the third day. In the object recognition test, the animals were allowed to explore two identical objects for 5 min in the sample phase (Trial 1). After the retention interval (1 h), animals were returned to the same open-field arena where one of the objects was replaced with a novel object in the 5 min test phase (Trial 2). The positions of the novel object in the test phase were counterbalanced. Relative preference for the novel object was calculated as the recognition index divided by the time spent exploring the new object by the total object exploration time.

Assessment for motor function of mice pups. As described in previous reports (Damseh et al., 2015; Kaplan et al., 2018), all tests were conducted in postnatal day 8 (P8) mice pups of nine different litters, respectively, from WT, CSMD3$^{-/-}$, and CSMD3$^{+/-}$ groups, and the average of three trials with a minimum of 30 min of rest between each trial was recorded. Ambulation was recorded by scoring ambulation according to the following scores: 0, no movement; 1, slow crawling with asymmetric limb movement; 2, slow crawling with symmetric limb movement; and 3, fast crawling. Righting reflex was monitored by recoding the time latency for the pups to turn over after they were put on their backs. Grip strength was measured by placing the mice on an iron mesh that was slowly adjusted to steeper angles. The angle in which the mice slipped was recorded. Hindlimb posture and suspension tests were completed by laying the mice suspended by their hindlimbs in padded 50 ml plastic conical tube and recording both the posture of the hindlegs and the latency to fall. Posture was scored as follows: 1, clasping of the hindlimbs; 2, hindlimbs very close or frequently touching each other; 3, hindlimbs closer but not touching each other; and 4, natural separation of hindlegs.

Rotarod test. The rotarod test was performed according to the method described previously (Liang et al., 2019). Briefly, mice first underwent a training procedure in which the animals were placed on a rotating drum with a constant speed of 4 rpm, forcing them to walk forward to avoid falling. Training sessions were conducted 1 and 2 d before the experiments, with three trials per day, with a minimum of 30 min intertrial rest intervals. In the testing procedure, the rod was accelerated from 4 to 40 rpm over 5 min. Latencies of animals (in seconds) to their first fall were recorded with a cutoff time of 300 s. The resulting data represent the mean amount of time each animal stayed on the rotarod across three trials, with a minimum of 30 min of rest between each trial. The rod was cleaned with 75% ethanol before the next animal was tested.

Open field test. According to the method described in a previous study (Kaplan et al., 2018), mice were placed in a white lusterless Perspex box (length, 50 cm; width, 50 cm; height, 40 cm) in a dark room for 30 min moving freely, videotaped by a digital camera and analyzed by a Smart 3.0 video-tracking system. The total distance traveled in 30 min was recorded for evaluating motor function.

Elevated plus maze test. According to the method described in previous study (Qi et al., 2022), the elevated plus maze (EPM) test was performed on the next day of the open field test (OFT). The maze consisted of two open arms and two closed arms (5 × 30 cm and a wall height of 15 cm for the closed arms) was placed 50 cm above the floor in a 60 lux illuminated room. Each mouse was placed in the center area heading toward the same open arm, and they were videotaped in the following 5 min. The time spent, the number of entries into open arms, and the total distance were analyzed using the SMART software. The maze was cleaned by 75% ethanol between tests.

Stereotaxic injection

Briefly, for intracranial virus injection, mice were anesthetized with pentobarbital sodium (10 mg/kg, i.p.) and placed on a stereotaxic frame (RWD Life Science). The skull surface was cleaned with 0.3% H_2O_2 followed by sterile saline on a sterilized cotton swab. For the *in vivo* fiber photometry calcium recording, AAVs including the mixture of rAAV2/9-VGAT1-Cre (catalog #PT-0346, BrainVTA; specific recognition to GABAergic neurons) with rAAV2/9-EF1α-DIO-GCaMP6s (catalog #PT-0071BrainVTA) or rAAV2/9-L7-GCaMP6s (catalog #PT-3318, BrainVTA; specific recognition to Purkinje cells) were stereotaxically injected into the Crus I/II lobules [distance from bregma: anteroposterior, −6.48 mm; mediolateral, ±1.50 mm; dorsoventral, −0.63 mm] in a volume of 400 nl at 50 nl/min, for specifically labeling of the cerebellar GABAergic cells and Purkinje cells, respectively. An optical fiber (outer diameter, 200 μm; numerical aperture, 0.37) housed in a ceramic ferrule was implanted ~0.1 mm above the injection site. For sparse labeling, diluted AAVs were stereotaxically injected into the Crus I/II lobules (distance from bregma: anteroposterior, −6.48 mm; mediolateral, ±1.50 mm; dorsoventral, −0.63 mm) in a volume of 400 nl at 50 nl/min. After injection, needles were left in place for an additional 5 min before it was slowly withdrawn to minimize the spread of viral particles along the injection tract. Then, skin was sutured and mice were put on a heating blanket before returning to their home cages. Mice were given 2–3 weeks for recovery from surgery and virus expression. Injection sites were verified histologically.

In vivo *fiber photometry calcium recording*

As a calcium indicator, GCaMP6s can reflect transient alterations of neuronal activity with high sensitivity. In the current experiment, *in vivo* Ca^{2+} signals of the cerebellar neurons were recorded using a fiber photometry system (ThinkerTech) in freely behaving mice during a rotarod test. Fiber photometry was performed as described previously (Huang et al., 2021). Three weeks after virus injection, a fiber photometry system (ThinkerTech) was used for recording calcium fluorescence signals

←

and vermis (middle), whereas the CSMD3-expressing cells are not distributed following the pattern of zebrin-II (right). Scale bar, 100 μm. ***G***, ***H***, Distribution of CSMD3-expressing PCs in cerebellar hemisphere. ***G***, Double-immunofluorescence staining with CSMD3 (green) and CB (red) in cerebellar hemisphere (sagittal section). Scale bar, 500 μm. ***H***, Bar graph represents the percentage of CSMD3/CB-positive PCs throughout all lobules in cerebellar hemisphere. ***I***, ***J***, Distribution of CSMD3-expressing PCs in cerebellar vermis. ***I***, Double immunofluorescence staining with CSMD3 (green) and CB (red) in cerebellar vermis (sagittal section). Scale bar, 500 μm. ***J***, Bar graph represents the percentage of CSMD3/CB-positive PCs throughout all lobules in cerebellar vermis. Data are presented as the mean ± SEM, but for ***A*** and ***B*** are presented as the mean ± SD.

produced by an exciting laser beam from a 490 nm laser. For recording of the cerebellar GABA/Purkinje cells during mice movement, fiber photometry recordings were taken during the first 15 min of the baseline test on the static rotarod followed by a 15 min rolling rotarod at a constant speed of 4 rpm. *Post hoc* histology was used to confirm the correct site of optical fibers and the expression of GCaMP6s. Raw photometry data were exported from Cam-Fiber-Photometry to MATLAB .mat files for further analysis. For each session, the photometry signal F value was converted to $\Delta F/F$ calculated by $(F - F_0)/(F_0 - F_{offset})$, where F_0 is the average fluorescence in the baseline recording episode and Foffset refers to the fluorescence values of the testing environment. The data were represented by a curve and corresponding heatmaps.

Electrophysiological studies

Cerebellar slice preparation. After pentobarbital sodium anesthesia and decapitation, acute sagittal slices (~250–300 μm) of the right cerebellar hemisphere were prepared from 6- to 8-week-old mice. Slices were cut using a vibratome (catalog #VT1000S, Leica) equipped with stainless steel blades in an ice-cold sucrose-based artificial CSF (ACSF), in which NaCl was replaced by equiosmolar sucrose, and were immediately transferred to an incubation chamber filled with normal ACSF and maintained at 35.5°C for 30 min and then at room temperature before use. For recording, a single slice was transferred into a recording chamber perfused with working ACSF at 31 ± 1°C. An infrared-differential interference contrast microscope (model Axioskop 2, Zeiss) was used for visualization of individual cells in the slice. The normal ACSF contained the following (in mM): 125 NaCl, 26 $NaHCO_3$, 10 D-glucose, 3 KCl, 2 $MgSO_4$, 2 $CaCl_2$, and 1.25 NaH_2PO_4, at 310 mOsm and pH 7.4, and was bubbled with 95% O_2 and 5% CO_2. The working ACSF contained the following (in mM): (1) 10 D-AP5, 10 NBQX, and 50 PTX, for current-clamp recording; (2) 1 tetrodotoxin (TTX) and 100 PTX, for miniature EPSCs (mEPSCs) recording; (3) 50 PTX, for long-term depression (LTD) recording; and (4) 1 TTX and 5 NBQX, for miniature inhibitory postsynaptic currents (mIPSCs) recording.

Electrophysiological recording. Whole-cell patch-clamp recording was performed on PCs at room temperature using a Multiclamp 700B amplifier and Digidata 1440A digitizer with Axon Clampex software (Molecular Device). PCs of Crus I/II lobules were identified by their morphology and distribution. Patch pipettes were pulled from borosilicate glass capillaries with a tip resistance of 3–5 MΩ when filled with one of the following internal solution, the components of which are as follows (in mM): (1) 135 K-gluconate, 6 KCl, 4 NaCl, 0.5 EGTA, 10 HEPES, 3 MgATP, 0.5 Na_3GTP, and 5 Na_2 phosphocreatine, at pH 7.4 and 290 mOsm, for current-clamp recording; (2) 135 Cs-methanesulfonate, 10 CsCl, 10 HEPES, 2 TEACl, 2 QX-314, 0.5 EGTA, 3 MgATP, and 0.5 Na_3GTP, at pH 7.4 and 290 mOsm, for mEPSC and evoked EPSCs recordings; and (3) 145 CsCl, 10 HEPES, 2 QX-314, 0.5 EGTA, 3 MgATP, and 0.5 Na_3GTP, at pH 7.4 and 290 mOsm, for mIPSC recording (Zhou et al., 2017; Courtney and Christian, 2018). In addition, 0.2% biocytin was also added to the pipette solution for *post hoc* staining of the recorded PCs. Membrane currents and action potentials (APs) were measured with both pipette and membrane capacitance cancellation, filtered at 2 kHz, and digitized at 10 kHz. Resting membrane potential (RMP) was measured immediately after rupture of the cell membrane in whole-cell patch mode. Series resistance (R_s) was compensated 70% to 90%.

Under current-clamp mode, the spontaneous firing of PCs was first recorded in gap-free mode at the holding current of 0 pA and lasted for 1 min. To investigate evoked action potentials, cells were held at −70 mV to prevent spontaneous spike activity, and those cells with bias current >400 pA were discarded. A series of current pulses (duration, 500 ms) from 0 to 600 pA in 100 pA increments was delivered to PCs with an interval of 5 s. A hyperpolarizing current pulse (500 ms) at −50 pA was delivered to measure membrane input resistance (R_{in}). The amplitude of APs was measured from the threshold to the peak. The afterhyperpolarization (AHP) size was measured from AP threshold to the negative peak of the AHP. The AP widths were measured at half-width. The voltage threshold was measured in the first derivative of AP (dV/dt) considering the point where the velocity was close to 20 V/s.

Under voltage-clamp mode, mEPSCs and mIPSCs were recorded at a holding potential of −70 mV, with both pipette and membrane capacitance cancellation, filtered at 2 kHz, and digitized at 10 kHz. Membrane resistance and R_s were monitored continuously during all experiments, with >20% change in R_s resulting in the omission of that experiment. The offline analysis of mEPSCs and mIPSCs was conducted using MiniAnalysis version 6.0 (Synaptosoft). The criteria for inclusion were amplitude >6 pA and a rise time (10–90%) >1 ms. Overlapping events were rejected. To obtain EPSCs at the parallel fiber (PF)–PC synapse, a concentric bipolar tungsten electrode (FHC) was placed in the upper molecular level to reduce the risk of unintentional climbing fiber (CF) activation (Piochon et al., 2014). LTD of EPSCs at PF–PC synapses was induced by a conjunction of five parallel fiber pulses at 100 Hz and a 100 ms depolarization of PC to 0 mV, repeated 30 times with an interval of 2 s (Zhou et al., 2017).

Three-dimensional reconstruction and morphology quantified

After recording, brain slices containing biocytin-filled cells were fixed in 4% PFA immediately overnight at 4°C. After three washes in 0.01 M PBS, pH 7.4, and incubated in the blocking solution (5% donkey serum and 0.3% Triton X-100 in PBS) for 1 h at room temperature, slices were then incubated with the mouse anti-calbindin antibody (1:500) at 4°C for 24 h, and then in the secondary antibody (1:1000; Alexa Fluor 488-conjugated donkey anti-mouse IgG) and streptavidin (1:500; Alexa Fluor 546 conjugated) for 2 h at room temperature (Deng et al., 2020). Slices were then rinsed in PBS and mounted on slides. The z stack images (1 μm/image) were acquired with an oil-objective (40×) on a confocal microscope and processed using Imaris (BitplaneAG8).

The Imaris filament tracer pipeline can be applied on background subtraction to reconstruct neuron morphology by using Imaris Bitplane software. Sholl analysis was used to assess the morphologic structure of dendrites, in which the radius interval of each section was set to 10 μm, starting from 0 μm and ending at a 200 μm distance from the soma.

Experimental design and statistical analysis

The experimental design is illustrated in the figures and described in figure legends. Images were carefully selected to show the average effect obtained for each experimental condition. Statistical analyses were performed with GraphPad Prism 8.0 for Windows (GraphPad Software). All quantitative biochemical data and histologic staining are representative of at least three independent biological replicates. Two-tailed unpaired Student's t test was used for the comparison of the mean values between two groups. One-way ANOVA with Tukey's *post hoc* test or two-way ANOVA with Tukey's or Sidak's *post hoc* test as indicated in the text were used for multiple comparison. All data are reported as the mean ± SEM, and differences with $p < 0.05$ were considered statistically significant: $^*p < 0.05$; $^{**}p < 0.01$; $^{***}p < 0.001$.

Results

Distribution and molecular identification of CSMD3-expressing cells in the cerebellum

CSMD3 is a giant gene expressing mainly in fetal and adult brains (Shimizu et al., 2003). Previously, the gene expression analyses have revealed that CSMD3 mRNA is highly expressed in the subplate during embryonic stages and ubiquitously expressed in the postnatal cerebral cortex (Oeschger et al., 2012). By searching from Brain RNA-Seq database (http://www.brainrnaseq.org/), we found that the CSMD3 mRNA is mainly expressed in neurons and oligodendrocytes (Fig. 1*A*,*B*). Using immunostaining of CSMD3 in cultured hippocampal neurons of embryonic mice, as well as in cultured MO3.13 cells (human oligodendrocytes), an immortalized human–human hybrid line that expresses the phenotypic characteristics of primary oligodendrocytes, including intracellular immunoreactivity for MBP (McLaurin et al., 1995), we indeed found a coexpression of CSMD3 with NeuN (a neuron marker) and MBP (an oligodendrocyte marker), respectively, in fetal mice cortical neurons and MO3.13 cells (Fig. 1*C*), validating the expression of

CSMD3 in neurons and oligodendrocytes. Moreover, the qRT-PCR and immunohistochemical staining data revealed that the CSMD3 was highly expressed in the cerebellum at mRNA (1.83 ± 0.38; $n = 6$) and protein levels (Fig. 1*D*,*E*). High-magnification images showed that the CSMD3-expressing cells were located in the PC layer (PCL), as well as in molecular layer (ML) and granular layer (GL) of the cerebellar cortex (Fig. 1*F*), where a discontinuous pattern of CSMD3-expressing PCs was observed, and also, the expression of CSMD3 did not match the expression pattern of zebrin stripe as indicated by the immunostaining of zebrin, the marker of cerebellar zonal expression (Fig. 1*F*). To further verify the expression of CSMD3 in PCs, the percentage of CSMD3-positive cells coexpressed with CB (a marker of cerebellar PCs)-positive cells was analyzed in all lobules in both cerebellar hemisphere and vermis (Fig. 1*G–J*). The results showed that a high proportion of PCs were coexpressing CSMD3 in all lobules (Fig. 1*H*,*J*). Compared with hemisphere (~66%; $n = 3$–4 slices from 3 mice; Fig. 1*H*), there was a higher percentage of CSMD3-positive PCs in vermis (~78%; $n = 4$ slices from 3 mice; Fig. 1*J*).

Then, the cell type-specific expression of CSMD3 was examined using double-immunofluorescence staining with different cell markers. The results revealed that except for PCs, CSMD3 was also expressed in NeuN-positive granular cells (Fig. 2*A*), CR-positive unipolar brush cells (Fig. 2*B*), and PV-positive inhibitory interneurons of the molecular layer (Fig. 2*C*). In addition, the colocalization of CSMD3 with MBP (Fig. 2*D*) but not Iba1 (Fig. 2*E*) or GFAP (Fig. 2*F*) was found, indicating that the CSMD3 was expressed in oligodendrocytes, but not in microglia or astrocytes. Altogether, these data suggest that the CSMD3 is preferentially expressed on both neurons (e.g., Purkinje cells, granular cells, interneurons, unipolar brush cells) and oligodendrocytes in cerebellar hemisphere and vermis.

Clinically, mutations of the *CSMD3* gene have been found in some autistic patients (Floris et al., 2008), suggesting that loss of CSMD3 expression likely contributes to the pathology of ASD. To determine the involvement of *CSMD3* deficiency in cerebellar dysfunction and the pathogenesis of ASD, we generated $CSMD3^{-/-}$ mice, which showed a lack of CSMD3 expression on calbindin-positive PCs (Fig. 2*H*,*I*) as well as a growth delay, including a decreased body weight gain ($n = 9$/group; $p < 0.0001$, wild type vs $CSMD3^{-/-}$; $F_{(18,216)} = 5.71$; Fig. 2*J*), using the CRISPR/Cas9 system (Fig. 2*G*).

CSMD3-deficient mice exhibit autism-like behaviors and motor impairments

Based on this mouse model, we sought to characterize the social behavior of the *CSMD3*-deficient mice in the three-chamber social task, a test broadly used for assessing mouse sociability and interest in social novelty (Crawley, 2007; Moy et al., 2009). As expected, the $CSMD3^{-/-}$ mice displayed impaired social interaction behaviors, as measured by assessing social preference and social novelty (Fig. 3*A–G*). Notably, the $CSMD3^{-/-}$ mice showed a significant loss of preference for the S1 mice, whereas the wild-type mice and the heterozygous ($CSMD3^{+/-}$) mice spent more time for interacting with S1 (S1: $n = 6$/group; wild type, 20.48 ± 4.11%; vs $CSMD3^{+/-}$, 16.47 ± 3.34%; vs $CSMD3^{-/-}$, 9.61 ± 2.78%; $p = 0.8637$; wild type vs $CSMD3^{+/-}$, $p = 0.0470$; wild type vs $CSMD3^{-/-}$, $F_{(2,30)} = 2.64$; Fig. 3*A*,*B*) than the objective (O; O: $n = 6$/group; wild type, 5.23 ± 0.81%; vs $CSMD3^{+/-}$, 5.40 ± 0.530%; vs $CSMD3^{-/-}$, 5.75 ± 0.96%; $p = 0.0021$; wild type: S1 vs O, $p = 0.0415$; $CSMD3^{+/-}$: S1 vs O, $p = 0.8818$; $CSMD3^{-/-}$: S1 vs O, $F_{(2,30)} = 2.64$; Fig. 3*A*,*B*), indicating impaired social preference in the $CSMD3^{-/-}$ mice. Moreover, in the social novelty test, the wild-type mice showed a significant preference for interacting with new stranger mice (S2; 19.52 ± 3.37%) than with the familiar mice (S1; 6.22 ± 1.35%; $n = 6$/group; wild type, $p = 0.0038$; S1 vs S2, $F_{(2,30)} = 4.43$; Fig. 3*A*,*C*), whereas the $CSMD3^{-/-}$ mice and the $CSMD3^{+/-}$ mice spent more time with the familiar mice (S1; $CSMD3^{-/-}$, 8.25 ± 1.84%; $CSMD3^{+/-}$, 8.80 ± 1.78%) and less time with the stranger mice (S2; $CSMD3^{-/-}$, 7.89 ± 1.82%; $CSMD3^{-/-}$, 14.24 ± 2.97%; $n = 6$/group, $p = 0.0142$; S2: wild type vs $CSMD3^{-/-}$, $F_{(2,30)} = 4.43$; Fig. 3*A*,*C*), suggesting impaired social novelty in *CSMD3*-deficient mice. Indeed, as normalized by social preference index and social novelty index, calculated as [interacting time in S1 chamber/(interacting time in S1 chamber + sniffing time in objective chamber)] and [interacting time in S2 chamber/(total interacting time in S1 and S2 chamber)], respectively, a statistical decrease in the social novelty index (wild type, 49.53 ± 8.13%; $CSMD3^{-/-}$, −5.06 ± 15.08%; $CSMD3^{+/-}$, 24.28 ± 4.98%; $n = 6$/group, $p = 0.0052$; wild type vs $CSMD3^{-/-}$, $F_{(2,15)} = 7.03$; Fig. 3*E*) and a decreased tendency in the social preference index (wild type, 55.95 ± 8.93%; $CSMD3^{-/-}$, 16.48 ± 16.80%; $CSMD3^{+/-}$, 38.41 ± 12.73%; $n = 6$/group, $p = 0.1209$; wild type vs $CSMD3^{-/-}$, $F_{(2,15)} = 2.24$; Fig. 3*D*) were observed in the $CSMD3^{-/-}$ mice, further validating the decreased sociability and social novelty preference in the *CSMD3*-deficient mice. In contrast, no significant difference in chamber entries was observed across three groups in both sociability test (S1: wild type, 26.17 ± 2.60; $CSMD3^{-/-}$, 17.50 ± 2.55; $CSMD3^{+/-}$, 36.83 ± 8.59; O: wild type, 15.67 ± 2.89; $CSMD3^{-/-}$, 22.83 ± 4.38; $CSMD3^{+/-}$, 27.83 ± 4.74; $n = 6$/group, $F_{(2,30)} = 1.67$; Fig. 3*F*) and social novelty test (S2: wild type, 25.67 ± 2.94; $CSMD3^{-/-}$, 13.83 ± 3.09; $CSMD3^{+/-}$, 20.17 ± 2.32; S1: wild type, 17.83 ± 1.96; $CSMD3^{-/-}$, 16.83 ± 4.09; $CSMD3^{+/-}$, 23.50 ± 3.00; $n = 6$/group, $F_{(2,30)} = 2.28$; Fig. 3*G*), suggesting that the exploratory activity is not impaired. Additionally, the self-grooming test revealed that both the $CSMD3^{-/-}$ and $CSMD3^{+/-}$ mice showed increased self-grooming time ($CSMD3^{-/-}$, 90.15 ± 8.94 s; $CSMD3^{+/-}$, 65.11 ± 13.65 s) compared with the wild-type mice (24.15 ± 5.06 s; $n = 9$/group; wild type vs $CSMD3^{-/-}$, $p = 0.0002$; wild type vs $CSMD3^{+/-}$, $p = 0.0190$; $F_{(2,24)} = 11.41$; Fig. 3*H*), indicating repetitive and stereotyped behavior in *CSMD3*-deficient mice. In contrast, the marble-burying test showed that both the $CSMD3^{-/-}$ mice (1.73 ± 0.86; $n = 11$) and the $CSMD3^{+/-}$ mice (1.69 ± 0.56 $CSMD3^{+/-}$; $n = 13$) buried significantly fewer marbles than the wild-type mice (4.78 ± 0.78; $n = 9$; wild type vs $CSMD3^{-/-}$, $p = 0.0226$; wild type vs $CSMD3^{+/-}$, $p = 0.0163$; $F_{(2,30)} = 5.30$; Fig. 3*I*) across all time points observed during a 25 min observation period. Consistently, reduced marble burying has been found in other autistic mice in previous studies (Gilbert et al., 2020; Suliman-Lavie et al., 2020). It has been documented that marble burying depends on interest in the external environment and that burying behavior does not change with increased experience with the marbles or habituation to the marble-burying test (Thomas et al., 2009; Greco et al., 2013). These findings therefore suggest that loss of CSMD3 expression dramatically decreases the interest of the animal in the external environment, a phenotype consistent with ASD (Gilbert et al., 2020). Also, no significant difference in spontaneous digging time (wild type, 58.00 ± 7.63 s; $CSMD3^{-/-}$, 42.13 ± 6.89 s; $CSMD3^{+/-}$, 39.00 ± 8.55 s) was observed across three groups ($n = 7$–8/group; wild type vs $CSMD3^{-/-}$, $p = 0.3230$; wild type vs $CSMD3^{+/-}$, $p = 0.2261$; $F_{(2,19)} = 1.71$; Fig. 3*J*), illustrating that that there is no alteration of innate behaviors. Moreover, the decreased recognition index was found in

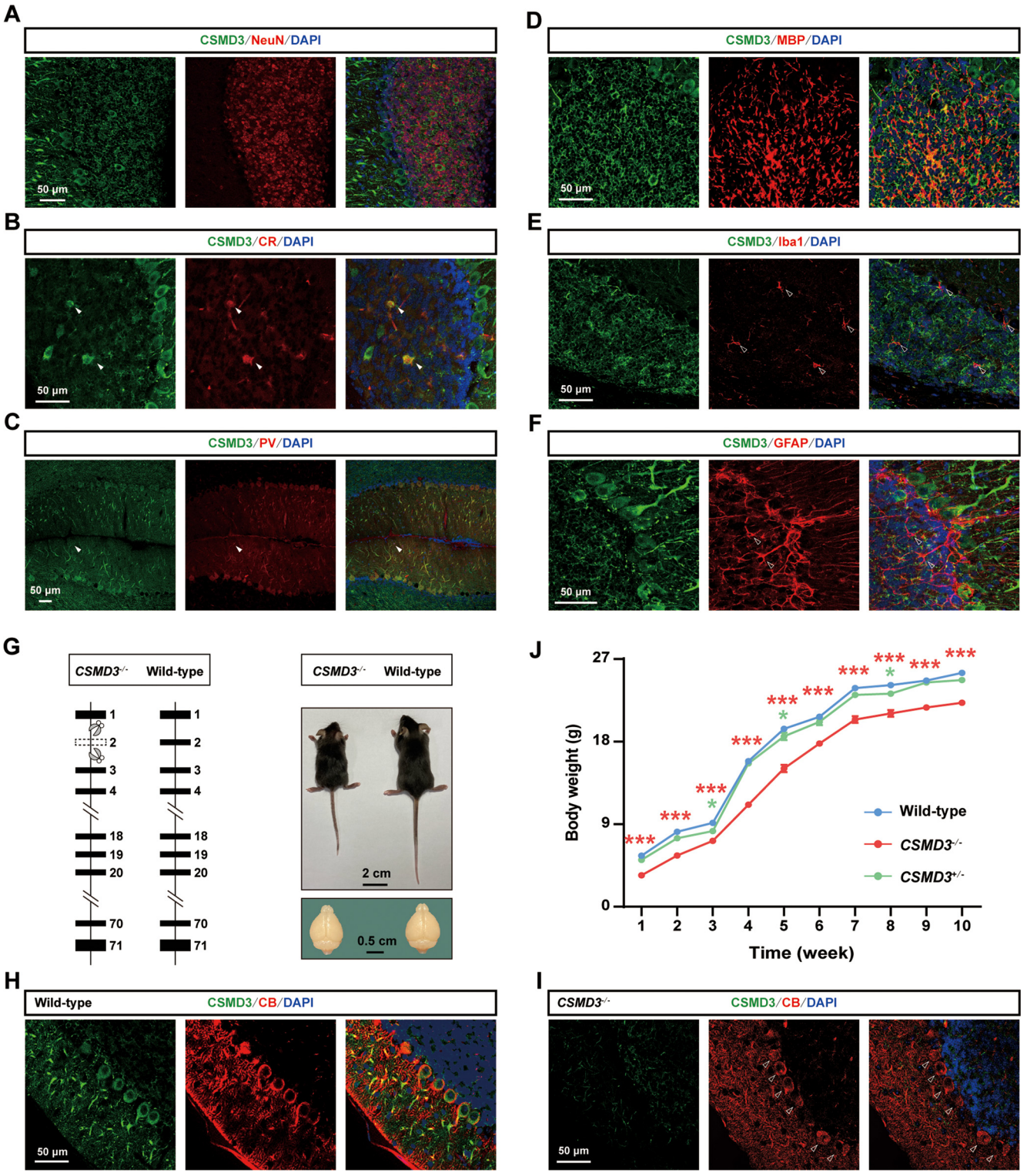

Figure 2. Molecular identity of cerebellar CSMD3-expressing cells and generation of *CSMD3*-mutant mice. ***A–F***, Molecular identity of cerebellar CSMD3-expressing cells. Immunofluorescence staining of CSMD3 with NeuN (***A***), CR (***B***), PV (***C***), MBP (***D***), Iba1 (***E***), or GFAP (***F***) and DAPI in the cerebellar cortex of wild-type mice. White arrowheads indicate cell localization in the cerebellar cortex. Scale bar, 50 μm. ***G–J***, Generation of *CSMD3* mutant mice. ***G***, Schematic illustrating the configuration for the generation of *CSMD3* mutation mice by using the CRISPR/Cas9 system. Exon 2 of a main spliceosome (*CSMD3*-201) was deleted to knock out the *CSMD3* gene (left), and photographs exhibiting the comparison of the body size and brain size between a male wild-type mouse and a male $CSMD3^{-/-}$ mouse at 6-week-old age (right). ***H***, ***I***, Immunofluorescence staining with CSMD3 (green), calbindin (red), and DAPI (blue) in the cerebellar cortex of wild-type (***H***) and $CSMD3^{-/-}$ (***I***) mice. Scale bar, 50 μm. ***J***, Graph of the growth curve (body weight gain) in the wild-type, $CSMD3^{-/-}$, and $CSMD3^{+/-}$ mice ($n = 9$ mice/group; $F_{(18,216)} = 5.71$; $CSMD3^{-/-}$ vs wild type, $p < 0.0001$; $CSMD3^{+/-}$ vs wild type, $p < 0.05$; two-way repeated-measures ANOVA with Tukey's *post hoc* test). Data are presented as the mean ± SEM: $^{*}p < 0.05$, $^{***}p < 0.001$.

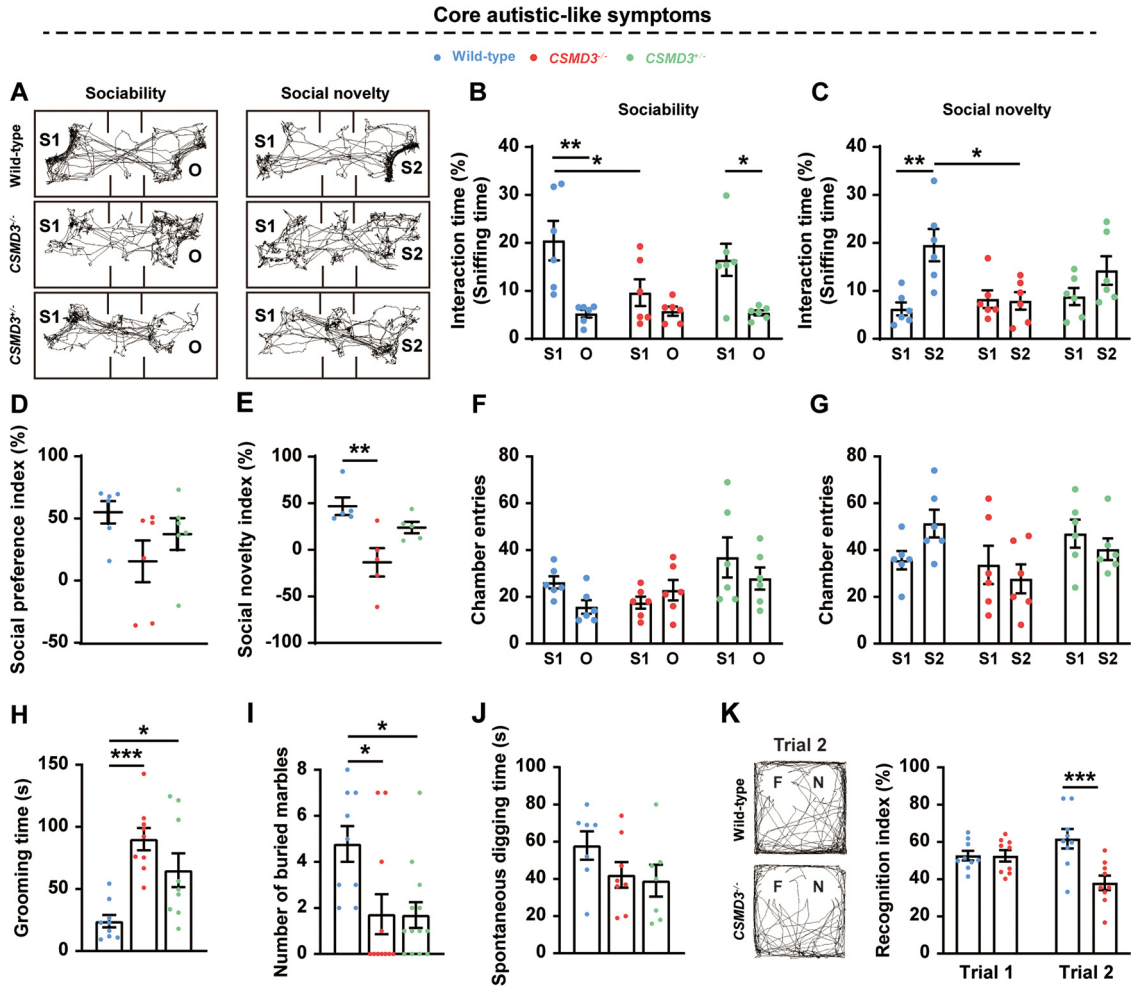

Figure 3. *CSMD3*-deficient mice exhibit core autistic-like symptoms. ***A–G***, Three-chamber sociability test. ***A***, representative automated tracking of a single mouse in the three-chamber sociability test (10 min duration in each stage) across the WT, $CSMD3^{-/-}$, and $CSMD3^{+/-}$ mice. ***B–G***, Bar graph represents sociability (***B***), social novelty (***C***), social preference index (***D***), social novelty index (***E***), as well as chamber entries in sociability test (***F***), and social novelty test (***G***): $F_{(2,30)} = 2.64$ (***B***), $F_{(2,30)} = 4.43$ (***C***), $F_{(2,15)} = 2.24$ (***D***), $F_{(2,15)} = 7.03$ (***E***), $F_{(2,30)} = 1.67$ (***F***), and $F_{(2,30)} = 2.28$ (***G***). ***H***, Grooming behaviors. ***I***, Marble-burying test. ***J***, Spontaneous digging behaviors. $F_{(2,24)} = 11.41$, $p = 0.0002$ and $p = 0.0019$ (***H***); $F_{(2,30)} = 5.30$, $p = 0.0226$ and $p = 0.0163$ (***I***); $F_{(2,19)} = 1.71$, $p = 0.3230$ and $p = 0.2261$ (***J***), $CSMD3^{-/-}$ versus WT and $CSMD3^{+/-}$ versus WT, respectively. ***K***, NOR test. Representative automated tracking of either a single wild-type or $CSMD3^{-/-}$ mouse in the NOR test (in the 5 min test phase, Trial 2; left) and bar graph of recognition index (right) are shown. $F_{(1,16)} = 7.71$, $p = 0.0002$ for Trial 2, $CSMD3^{-/-}$ versus WT. Data are presented as the mean ± SEM: $n = 6$ mice/group (***B–G***); $n = 9$–13 mice/group (***H–K***). $^*p < 0.05$, $^{**}p < 0.01$, and $^{***}p < 0.001$, two-way ANOVA with Tukey's *post hoc* test (***B***, ***C***, ***F***, ***G***); two-way ANOVA with Sidak's *post hoc* test (***K***); one-way ANOVA with Tukey's *post hoc* test (***D***, ***E***, ***H–J***).

$CSMD3^{-/-}$ mice (38.02 ± 3.88%) compared with wild-type mice (61.67 ± 5.25%) in the NOR test (wild type vs $CSMD3^{-/-}$ for trial 2, $p = 0.0002$) with no recognitive preference (wild type, 52.64 ± 2.57%; vs $CSMD3^{-/-}$, 52.50 ± 3.06%; wild type vs $CSMD3^{-/-}$ for trial 1, $p = 0.9996$) during the sample phase, in which the mice were allowed to explore the same two identical objects ($n = 9$/group; $F_{(1,16)} = 7.71$; Fig. 3*K*), validating the decreased novelty-seeking activity, one of the core symptoms in ASD. Together, these findings suggest that the *CSMD3*-deficient mice display core autistic-like symptoms, including deficits in social interaction, repetitive behaviors, and restricted interests.

In addition to the core autistic-like symptoms, anxiety is a frequent symptom associated with ASD patients (van Steensel et al., 2011). Therefore, OFT and EPM test were applied to measure anxiety-like behaviors in *CSMD3*-mutant mice. Although no significant difference was observed in time spent in the center (wild type, 108.50 ± 22.44 s; $CSMD3^{-/-}$, 67.07 ± 13.01 s; $CSMD3^{+/-}$, 88.71 ± 33.07 s) across the wild type, $CSMD3^{-/-}$, and $CSMD3^{+/-}$ mice in the OFT ($n = 4$–6/group; wild type vs $CSMD3^{-/-}$, $p = 0.5666$; wild type vs $CSMD3^{+/-}$, $p = 0.8648$; $F_{(2,12)} = 0.55$; Fig. 4*A*,*B*), the homozygous ($CSMD3^{-/-}$) mice spent significantly less time exploring the open arms than did the wild-type mice in the EPM test (wild type, 77.78 ± 20.58 s; $CSMD3^{-/-}$, 11.98 ± 6.44 s; $CSMD3^{+/-}$, 34.83 ± 8.83 s; $n = 4$–6/group; wild type vs $CSMD3^{-/-}$, $p = 0.0073$; wild type vs $CSMD3^{+/-}$, $p = 0.0628$; $F_{(2,12)} = 7.11$; Fig. 4*C*,*D*). Moreover, both the $CSMD3^{-/-}$ and $CSMD3^{+/-}$ mice exhibited reduced entries in the open arms (wild type, 11.50 ± 3.12; $CSMD3^{-/-}$, 2.00 ± 0.63; $CSMD3^{+/-}$, 4.33 ± 0.76; $n = 4$–6/group; wild type vs $CSMD3^{-/-}$, $p = 0.0038$; wild type vs $CSMD3^{+/-}$, $p = 0.0186$; $F_{(2,12)} = 9.00$; Fig. 4*E*), indicating anxiety-like behaviors in the *CSMD3* mutant mice. In addition, the $CSMD3^{-/-}$ mice also displayed serious motor function impairment, as evaluated either in the OFT or in the EPM test. For instance, the $CSMD3^{-/-}$ mice showed a significant decrease in the total distance traveled (wild type, 137.70 ± 10.78 m; $CSMD3^{-/-}$, 93.21 ± 5.46 m; $CSMD3^{+/-}$, 139.50 ± 7.34 m; $n = 4$–6/group; wild type vs $CSMD3^{-/-}$, $p = 0.0063$; $F_{(2,12)} = 11.54$; Fig. 4*F*) in the OFT, indicating a hypoactivity for the locomotor function. Likewise, both the

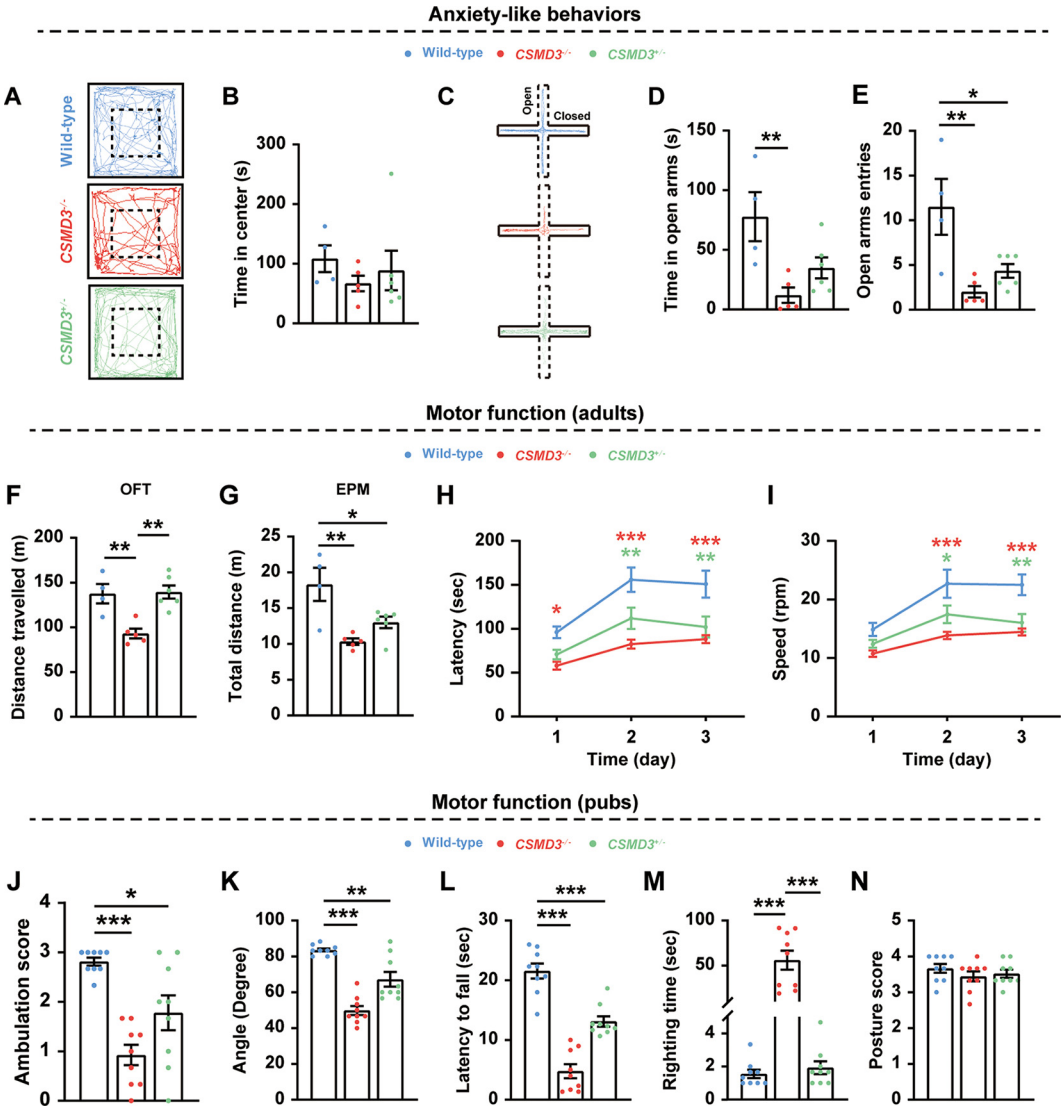

Figure 4. *CSMD3*-deficient mice exhibit anxiety-like behaviors and motor impairments. ***A–E***, Assessment of anxiety-like behaviors. ***A***, ***B***, OFT. ***A***, Representative automated tracking of a single mouse in the OFT (5 min duration) across the wild-type, $CSMD3^{-/-}$, and $CSMD3^{+/-}$ mice. ***B***, Bar graph shows time spent in the center. $F_{(2,12)} = 0.55$, $p = 0.5666$ and $p = 0.8648$, $CSMD3^{-/-}$ versus WT and $CSMD3^{+/-}$ versus WT, respectively. ***C–E***, EPM test. ***C***, Representative automated tracking of a single mouse in the EPM (5 min duration) across the wild-type, $CSMD3^{-/-}$, and $CSMD3^{+/-}$ mice. ***D***, Bar graph shows time spent in open arms. $F_{(2,12)} = 7.11$, $p = 0.0073$ and $p = 0.0628$, $CSMD3^{-/-}$ versus WT and $CSMD3^{+/-}$ versus WT, respectively. ***E***, Bar graph shows the number of open arms entries. $F_{(2,12)} = 9.00$, $p = 0.0038$ $CSMD3^{-/-}$ versus WT; $p = 0.0186$ $CSMD3^{+/-}$ versus WT. ***F–I***, Assessment of adult motor function. ***F***, Bar graph shows total distance traveled in OFT; $CSMD3^{-/-}$ versus WT: $F_{(2,12)} = 11.54$, $p = 0.0063$; $CSMD3^{-/-}$ versus $CSMD3^{+/-}$, $p = 0.0022$; ***G***, Bar graph shows total distance traveled in EPM; $CSMD3^{-/-}$ versus WT, $F_{(2,12)} = 9.89$, $p = 0.0023$; $CSMD3^{+/-}$ versus WT, $p = 0.0256$. ***H***, ***I***, Rotarod test; line graphs show the latency (***H***) and speed (***I***) at which the mice fall from the rod: $F_{(4,24)} = 1.90$ (***H***); $F_{(4,24)} = 2.54$ (***I***). ***J–N***, Assessment of the motor function of pups: ambulation score (***J***); angle to fall (***K***); latency to fall (***L***); righting time (***M***); posture score (***N***). $F_{(2,24)} = 15.56$, $p < 0.0001$ and $p = 0.0144$ (***J***); $F_{(2,24)} = 35.87$, $p < 0.0001$ and $p = 0.0012$ (***K***); $F_{(2,24)} = 57.77$, $p < 0.0001$ and $p < 0.0001$ (***L***); $F_{(2,24)} = 26.86$, $p < 0.0001$ and $p = 0.9990$ (***M***); $F_{(2,24)} = 0.82$, $p = 0.4307$ and $p = 0.6822$ (***N***), $CSMD3^{-/-}$ versus WT and $CSMD3^{+/-}$ versus WT, respectively. Data are presented as the mean ± SEM; $n = 4$–6 mice/group (***A–I***); $n = 9$ mice/group (***J–N***); $^{*}p < 0.05$, $^{**}p < 0.01$, and $^{***}p < 0.001$, one-way ANOVA with Tukey's *post hoc* test (***B***, ***D–G***, ***J–N***); two-way ANOVA with Tukey's *post hoc* test (***H***, ***I***).

$CSMD3^{-/-}$ and $CSMD3^{+/-}$ mice exhibited a statistical decline in the total distance traveled in the EPM test (wild type, 18.31 ± 2.33 m; $CSMD3^{-/-}$, 10.32 ± 0.44 m; $CSMD3^{+/-}$, 13.00 ± 0.80 m) compared with the wild-type mice ($n = 4$–6/group; wild type vs $CSMD3^{-/-}$, $p = 0.0023$; wild type vs $CSMD^{+/-}$, $p = 0.0256$; $CSMD3^{-/-}$ vs $CSMD3^{+/-}$, $p = 0.2700$; $F_{(2,12)} = 9.89$; Fig. 4*G*). Supporting these findings, some clinical reports have shown that ASD patients often manifest deficits in motor coordination and delayed development of motor skills that are associated with the cerebellar function (Green et al., 2009; Fournier et al., 2010; Harris, 2017; Wilson et al., 2018). To further determine this understanding, the rotarod test was performed to assess motor coordination and cerebellum-dependent motor learning by placing animals on an accelerating rod. The results revealed that there was a significant difference in the latency to fall on day 1 between the $CSMD3^{-/-}$ mice and the wild-type mice (wild type, 95.94 ± 6.65 s; $CSMD3^{-/-}$, 58.00 ± 4.375 s; $CSMD3^{+/-}$, 70.71 ± 5.389 s; $n = 4$–6/group; wild type vs $CSMD3^{-/-}$, $p = 0.0332$; $F_{(3,24)} = 1.90$; Fig. 4*H*), indicating that the initial motor skill is impaired in $CSMD3^{-/-}$ mice. During the training phase (on day 2) and the testing phase (on day 3), both the latency (day 2: wild type, 155.80 ± 13.91 s; $CSMD3^{-/-}$, 82.50 ± 5.15 s; $CSMD3^{+/-}$, 111.90 ± 12.20 s; day 3: wild type, 150.80 ± 15.33 s; $CSMD3^{-/-}$, 88.10 ± 4.55 s; $CSMD3^{+/-}$, 101.90 ± 12.11 s) and the speed (in rpm; day 2: wild type, 22.69 ± 2.39; $CSMD3^{-/-}$, 13.85 ± 0.62; $CSMD3^{+/-}$, 111.90 ± 12.20 s; day 3: wild type, 150.80 ± 15.33 s; $CSMD3^{-/-}$, 88.10 ± 4.55 s; $CSMD3^{+/-}$,

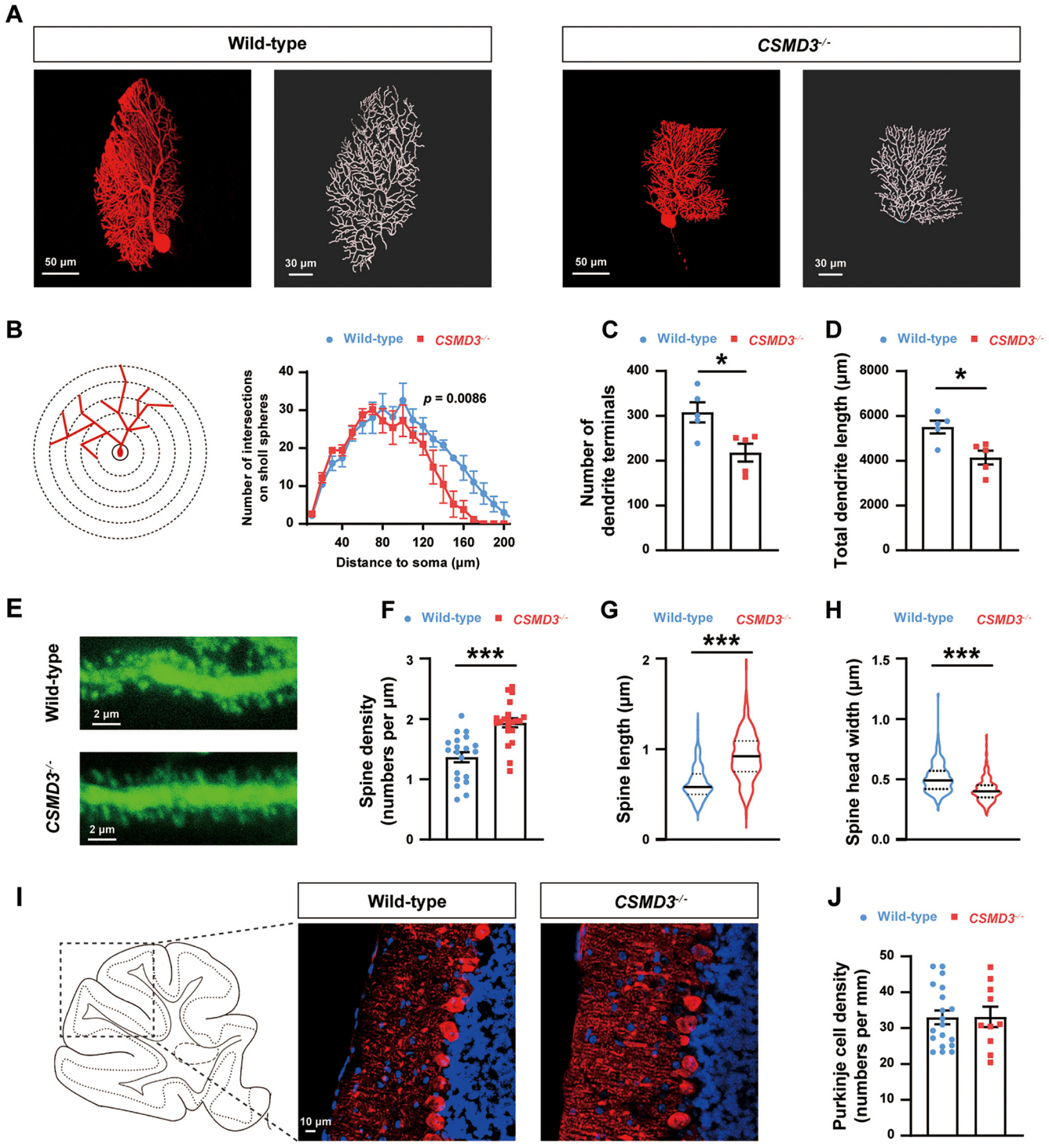

Figure 5. *CSMD3*-deficient mice display abnormal cerebellar PCs morphology. ***A***, Representative images showing the biocytin-labeled PCs (red) and the 3D reconstruction of PCs morphology (gray) in the WT (left) and *CSMD3*$^{-/-}$ (right) mice. Scale bars: 50 µm (red); 30 µm (gray), respectively. ***B***, Sholl analysis of the biocytin-labeled PCs. Left, Representative PC with concentric circles used for the Sholl analysis. The radius interval between the circles was set to 20 μm/step, ranging from 40 to 200 μm, from the center of the neuronal soma to the end of the dendrites. Right, Quantified analysis of the numbers of dendritic intersections per circle ($n = 5$ cells from 3 mice/group; *CSMD3*$^{-/-}$ vs WT: $F_{(21,168)} = 1.92$, $p = 0.0086$). ***C***, ***D***, Quantified analysis of dendrite terminals (***C***) and total dendrite length (***D***) in the wild-type and *CSMD3*$^{-/-}$ mice ($n = 5$ cells from 3 mice/group; $t_{(8)} = 3.0$, $p = 0.0172$ (***C***); $t_{(8)} = 3.24$, $p = 0.0119$ (***D***), *CSMD3*$^{-/-}$ vs WT). ***E***, Representative images showing the spines on EGFP-positive PC dendrites in the WT (top) and *CSMD3*$^{-/-}$ (bottom) mice. Scale bar, 2 µm. ***F***, Quantified analysis of dendritic spine density in the wild-type and *CSMD3*$^{-/-}$ mice ($n = 20$–21 dendrites from 7–8 mice/group; $t_{(39)} = 4.99$, $p < 0.0001$). ***G***, Quantified analysis of dendritic spine length in the wild-type and *CSMD3*$^{-/-}$ mice ($n = 164$–231 spines from 3 mice/group; $t_{(393)} = 12.27$, $p < 0.0001$). ***H***, Quantified analysis of dendritic spine head width in the wild-type and *CSMD3*$^{-/-}$ mice ($n = 164$–231 spines from 3 mice/group; $t_{(393)} = 8.61$, $p < 0.0001$). ***I***, Representative images showing the immunofluorescent staining with calbindin (the cerebellar PC marker; red) and DAPI (the nuclear marker; blue) in sagittal cerebellar sections obtained from the wild-type (left) and *CSMD3*$^{-/-}$ (right) mice. Scale bar, 10 µm. ***J***, Quantified analysis of PC density in cerebellar Crus I/II lobules in WT and *CSMD3*$^{-/-}$ mice ($n = 10$–19 slices from 3–5 mice/group; *CSMD3*$^{-/-}$ vs WT: $t_{(27)} = 0.03$, $p = 0.9767$). Data are presented as the mean ± SEM. *$p < 0.05$, **$p < 0.01$, and ***$p < 0.001$, two-way repeated-measures ANOVA with Sidak's *post hoc* test (***B***); two-tailed unpaired *t* test (***C***, ***D***, ***F***, ***G***, ***H***, ***J***).

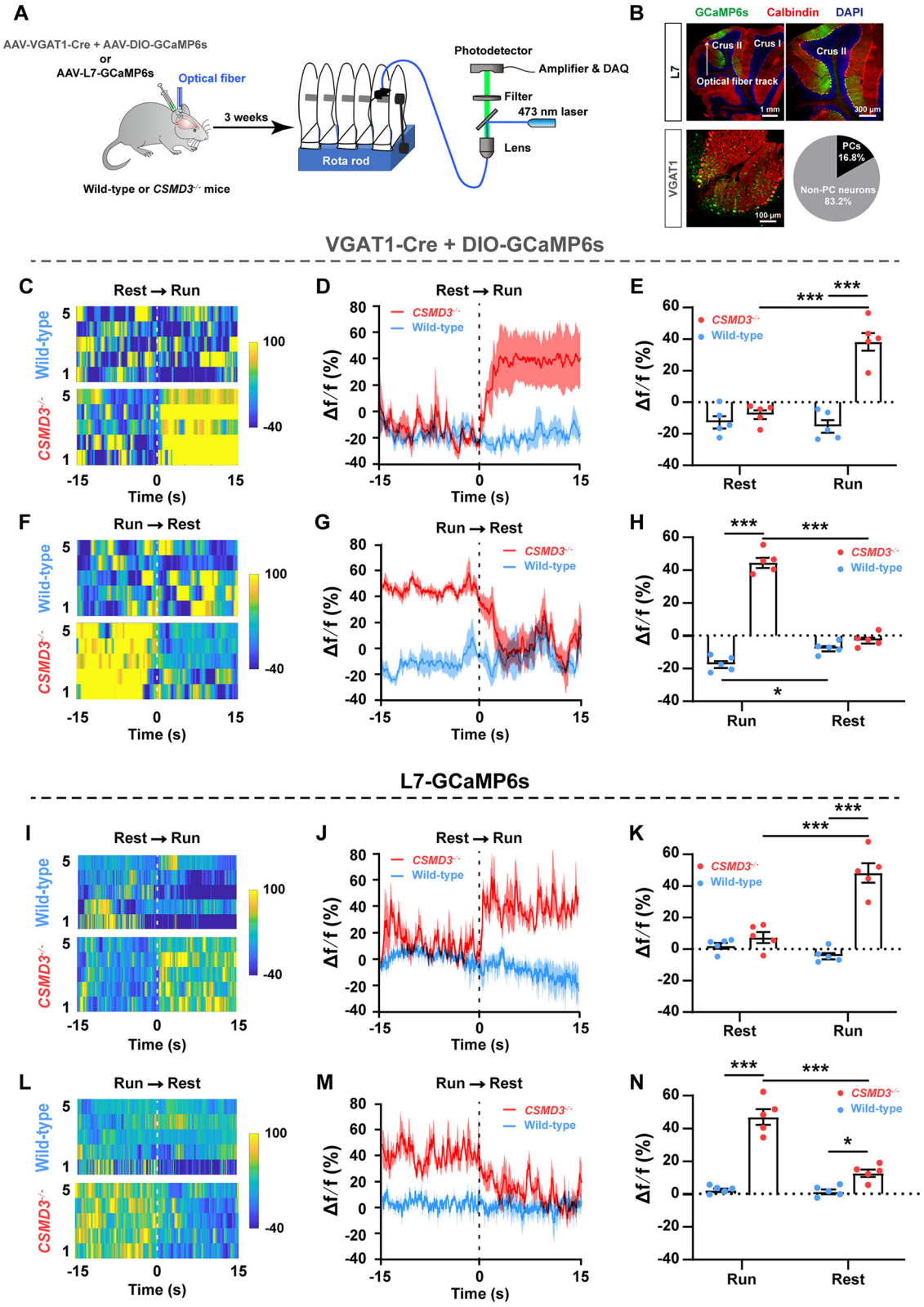

Figure 6. *CSMD3*-deficient mice manifest increased neuronal activity of cerebellar PCs in response to movement activity. ***A***, Schematic for virally expressed GCaMP6 in cerebellar GABAergic neurons or PCs in the Crus I/II lobules and the *in vivo* fiber photometry Ca^{2+} signal recording in freely moving mice during rotarod test. ***B***, Representative images of immunofluorescence staining with GCaMP6s (green) and calbindin (red)/DAPI (blue), illustrating GCaMP6s expression in cerebellar PCs at the placement of the tip of the fiber. Pie chart shows that 16.8% of the transfected cells by the AAV mix of VGAT1-Cre with DIO-GCamp6s are PCs. Scale bars: L7, left, 1 mm; L7, right, 300 μm; VGAT1, 100 μm. ***C–H***, Ca^{2+} fluorescent signals recorded from cerebellar GABAergic neurons in the Crus I/II lobules. ***I–N***, Ca^{2+} fluorescent signals recorded from cerebellar PCs in the Crus I/II lobules. ***C***, ***F***, ***I***, ***L***, Heat map depicting changes in the Ca^{2+} signals of cerebellar GABAergic neurons (***C***, ***F***) and PCs (***I***, ***L***) related to movement activity, respectively. ***C***, ***I***, from rest to run. ***F***, ***L***, from run to rest. Each row shows one trial for one mouse, and five traces are illustrated. Color scale at the right indicates $\Delta F/F$. ***D***, ***G***, ***J***, ***M***, Perievent plot of the averaged Ca^{2+} transients recorded from cerebellar GABAergic neurons (***D***,***G***) and PCs (***J***,***M***) in the wild-type (wathet blue) and *CSMD3*$^{-/-}$ (red) mice during rotarod test. ***D***, ***J***, From rest to run. ***G***, ***M***, From run to rest. Red (or wathet blue) thick lines indicate the mean, and shaded areas represent

17.46 ± 1.52) at which the *CSMD3*$^{-/-}$ mice fell from the rod were much lower than those of the wild type mice (n = 4–6/group; Fig. 4*H*: day 2, $p < 0.0001$; day 3, $p = 0.0003$; $F_{(4,24)} = 1.90$; Fig. 4*I*: day 2, $p = 0.0001$; day 3, $p = 0.0005$; $F_{(4,24)} = 2.54$) and also, the *CSMD3*$^{+/-}$ mice showed a lower latency and speed compared with the wild-type mice (n = 4–6/group; Fig. 4*H*: day 2, $p = 0.0089$; day 3, $p = 0.0034$; $F_{(4,24)} = 1.90$; Fig. 4*I*: day 2, $p = 0.0195$; day 3, $p = 0.0032$; $F_{(4,24)} = 2.54$), suggesting an impaired motor skill and learning ability in *CSMD3*-deficient mice.

In addition, we also monitored various motor functions of mouse pups at P8 to evaluate the time of onset of the disorder and the motor dysfunction at different ages. For mouse pups, we found that both the *CSMD3*$^{-/-}$ and *CSMD3*$^{+/-}$ mouse pups exhibited a decreased ambulation score, indicated by slow crawling and some asymmetric limb movements in the ambulation pattern assessment (wild type, 2.82 ± 0.08; *CSMD3*$^{-/-}$, 0.93 ± 0.21; *CSMD3*$^{+/-}$, 1.78 ± 0.35; Fig. 4*J*: n = 9/group; wild type vs *CSMD3*$^{-/-}$, $p < 0.0001$; wild type vs *CSMD3*$^{+/-}$, $p = 0.0144$; $F_{(2,24)} = 15.56$). When placed on an iron mesh that was gradually inverted, both *CSMD3*$^{-/-}$ and *CSMD3*$^{+/-}$ mouse pups fell at lower angels (wild type, 83.52 ± 0.94°; *CSMD3*$^{-/-}$, 49.81 ± 2.52°; *CSMD3*$^{+/-}$, 67.22 ± 4.06°; Fig. 4*K*: n = 9/group; wild type vs *CSMD3*$^{-/-}$, $p < 0.0001$; wild type vs *CSMD3*$^{+/-}$, $p = 0.0012$; $F_{(2,24)} = 35.87$) and exhibited shorter latency (wild type, 21.56 ± 1.25 s; *CSMD3*$^{-/-}$, 4.78 ± 1.17 s; *CSMD3*$^{+/-}$, 13.11 ± 0.86 s; Fig. 4*L*: n = 9/group; wild type vs *CSMD3*$^{-/-}$, $p < 0.0001$; wild type vs *CSMD3*$^{+/-}$, $p < 0.0001$; $F_{(2,24)} = 57.77$) to fall, indicating a weaker grip strength in the four limbs. Also, the *CSMD3*$^{-/-}$ mice pubs exhibited a delayed righting response when placed on their backs (wild type, 1.56 ± 0.25 s; *CSMD3*$^{-/-}$, 55.93 ± 10.44 s; *CSMD3*$^{+/-}$, 1.93 ± 0.39 s; Fig. 4*M*: n = 9/group; wild type vs *CSMD3*$^{-/-}$, $p < 0.0001$; $F_{(2,24)} = 26.86$), although these mouse pups display normal posture when suspended by their hindlegs at the rim of a conical tube (wild type, 3.67 ± 0.12; *CSMD3*$^{-/-}$, 3.44 ± 0.14; *CSMD3*$^{+/-}$, 3.52 ± 0.11; Fig. 4*N*: n = 9/group; wild type vs *CSMD3*$^{-/-}$, $p = 0.4307$; $F_{(2,24)} = 0.82$). These data suggest that the *CSMD3*-deficient mouse pups display a significant motor dysfunction compared with the wild-type mouse pups. Together, these results showed that, apart from the core autistic-like symptoms, other symptoms, including the anxiety-like behaviors and the motor dysfunction, were also exhibited in the *CSMD3*-deficient mice.

CSMD3-deficient mice display abnormal cerebellar PCs morphology

CSMD3 is implicated in the regulation of dendrite development, and malfunctions of CSMD3 may be one of the factors in the pathogenesis of psychiatric disorders (Mizukami et al., 2016). We thus speculated that loss of CSMD3 will impair cerebellar development especially the dendrite development of cerebellar PCs, which will subsequently lead to the dysfunction of the cerebellum and its associated motor dysfunction and the pathogenesis of ASD. To test this understanding, cerebellar slices containing biocytin-filled cells were applied to examine the morphology of PCs in the Crus I/II lobules. Analyses of three-dimensional (3D) reconstruction of biocytin-labeled PCs revealed that *CSMD3*$^{-/-}$ mice had stunted and smaller dendritic arbors in the cerebellar PCs compared with the wild-type mice (Fig. 5*A*). Moreover, Sholl analysis of the biocytin-labeled PCs showed that the PCs in the cerebellums of *CSMD3*$^{-/-}$ mice were smaller with less bifurcated dendritic branches ($p = 0.0086$, $F_{(1,8)} = 11.96$; Fig. 5*B*); and also, the number of dendrite terminals (wild type, 308 ± 22.51; vs *CSMD3*$^{-/-}$, 218.2 ± 19.81; $p = 0.0172$, $t_{(8)} = 2.30$; Fig. 5*C*) and the total dendrite length (wild type, 5505 ± 287.1 µm; vs *CSMD3*$^{-/-}$, 4143 ± 307.1 µm; $p = 0.0019$, $t_{(8)} = 3.24$; Fig. 5*D*) were both decreased in the cerebellar PCs in *CSMD3*$^{-/-}$ mice (n = 5 cells from 3 mice/group). Of note, by using a combination of immunofluorescent staining for the biocytin-labeled PCs, Golgi–Cox staining, and sparse labeling of PCs in the Crus I/II lobules for the cerebellar tissues, we found a robust increase in the dendritic spine density (in numbers/micron; wild type, 1.37 ± 0.08; vs *CSMD3*$^{-/-}$, 1.94 ± 0.08; n = 20–21 dendrites from 7–8 mice/group; $p < 0.0001$, $t_{(39)} = 4.99$; Fig. 5*E*,*F*) and the spine length (wild type, 0.63 ± 0.01 µm; vs *CSMD3*$^{-/-}$, 0.92 ± 0.02 µm; n = 164–231 spines from 3 mice/group; $p < 0.0001$, $t_{(393)} = 12.27$; Fig. 5*E*,*G*) of PCs in the Crus I/II lobules in *CSMD3*$^{-/-}$ mice. Nevertheless, the width of the spine head was significantly decreased in the *CSMD3*$^{-/-}$ mice (wild type, 0.51 ± 0.01 µm; vs *CSMD3*$^{-/-}$, 0.41 ± 0.01 µm) compared with the wild-type mice (n = 164-231 spines from 3 mice/group; $p < 0.0001$, $t_{(393)} = 8.61$; Fig. 5*H*). Unexpectedly, by using immunofluorescent staining with calbindin and DAPI, we did not observe significant difference in PCs numbers (PC density, in numbers/millimeter) between the *CSMD3*$^{-/-}$ mice and the wild-type mice (in numbers/millimeter; wild type, 33.01 ± 1.93; vs *CSMD3*$^{-/-}$, 33.11 ± 2.84; n = 10–19 slides from 3–5 mice; $p = 0.9767$, $t_{(27)} = 0.03$; Fig. 5*I*,*J*). These results suggest that loss of CSMD3 indeed results in abnormal cerebellar PC morphology because of the impairment of dendrite development.

CSMD3-deficient mice manifest increased neuronal activity of cerebellar PCs in response to movement activity

To further explore whether loss of CSMD3 also affect the functional activity of cerebellar PCs (a specific type of GABAergic neurons), we expressed GCaMP6s (a specific calcium indicator) respectively in cerebellar GABAergic cells and PCs in the Crus I/II lobules, and examined the *in vivo* real-time neuronal activity of these cells in freely moving mice during rotarod test, using fiber photometry with a calcium imaging system (Fig. 6). GCaMP6s were selectively expressed in cerebellar GABAergic cells and PCs in the Crus I/II lobules, respectively, using AAV infection, including a mix of rAAV2/9-VGAT1-Cre (specific recognition to GABAergic neurons) with rAAV2/9-EF1α-DIO-GCaMP6s (PCs made up 18.6% of the transfected neurons) or rAAV2/9-L7-GCaMP6s (specific recognition to Purkinje cells; Fig. 6*A*,*B*). CaMP6 green fluorescence signals (i.e., calcium fluorescence signals or calcium fluctuations), a measure of population neuronal activity, were monitored during rotarod test. A time-locked transient increase in calcium fluorescence signal intensity was observed in both GABAergic cells (n = 5 mice/group; rest: wild type, −12.80 ± 3.90%; vs *CSMD3*$^{-/-}$, −8.00 ± 2.78%; $p = 0.9654$; run: wild type, −15.40 ± 3.98%; vs *CSMD3*$^{-/-}$, 38.20 ± 5.59%; $p < 0.0001$, $F_{(1,16)} = 34.00$; Fig. 6*C*–*E*) and PCs (n = 5 mice/group; rest: wild type, 1.36 ± 1.49%; vs *CSMD3*$^{-/-}$, 5.45 ± 2.70%; $p = 9171$; run: wild type. −3.66 ± 1.53%;

←

the SEM (n = 5 mice/group). Dashed line indicates the transition point of the event. ***E***, ***H***, ***K***, ***N***, Comparison of the normalized calcium responses under rest and run conditions across the group of mice recorded (n = 5 mice/group; $F_{(1,16)} = 34.00$, ***E***; $F_{(1,16)} = 166.80$, ***H***; $F_{(1,16)} = 38.81$, ***K***; and $F_{(1,16)} = 37.81$, ***N***; two-way ANOVA with Sidak's *post hoc* test. $\Delta F/F$ represents the deviation in Ca^{2+} fluorescence from the baseline, which is the averaged $\Delta F/F$ between t of −15 and 0 s. Data are presented as the mean ± SEM. *$p < 0.05$, **$p < 0.01$, and ***$p < 0.001$.

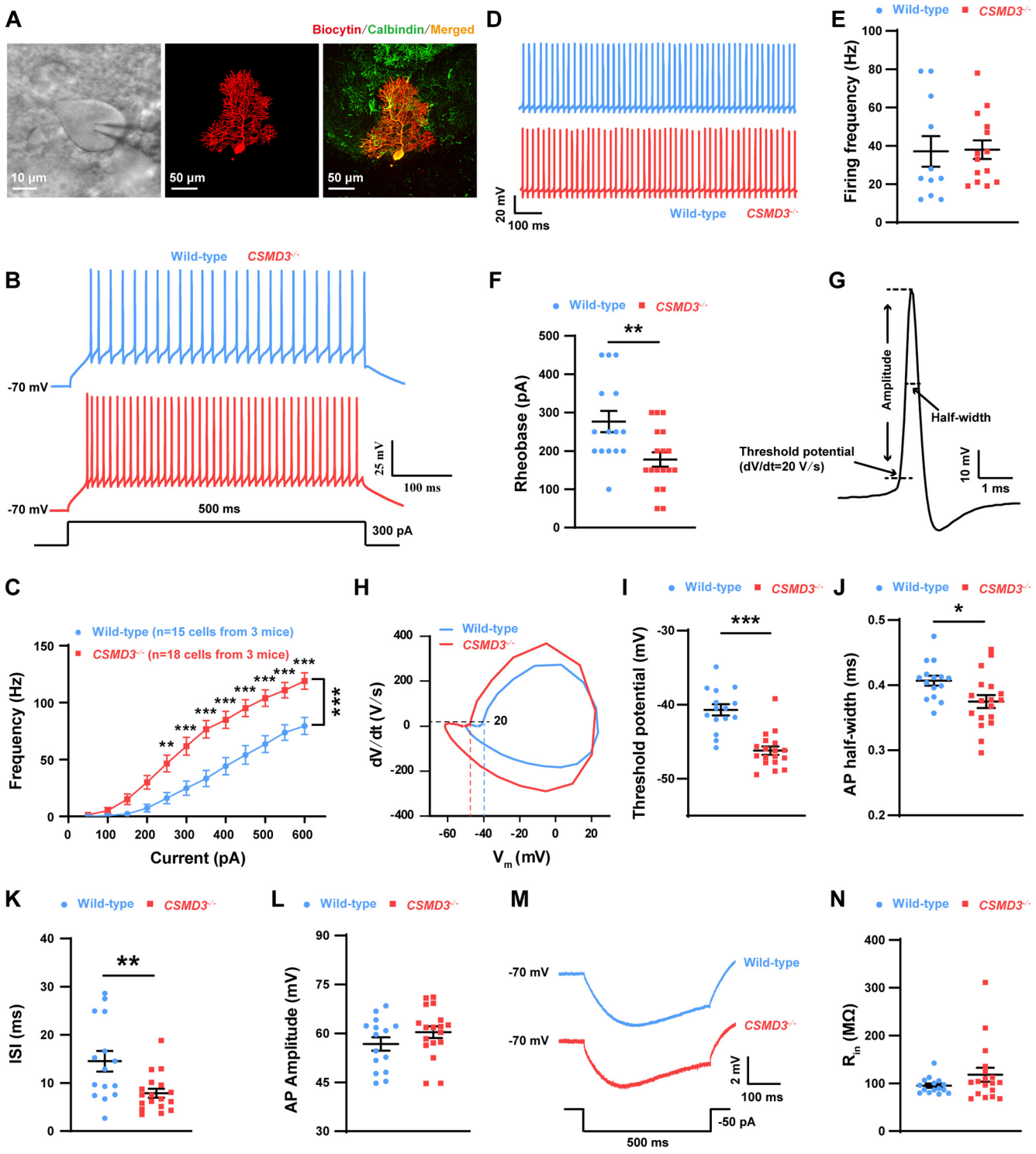

Figure 7. *CSMD3*-deficient mice manifest aberrant increased excitability in cerebellar PCs. ***A***, Representative images showing a patch-clamp recorded PC. Left, Light-field image of a patch-clamped cell; middle, biocytin labeling for the patch-clamp recorded cell (red); right, colocalization of biocytin with calbindin (cerebellar PCs marker, green) immunostaining. Scale bars: left, 10 μm; middle and right, 50 μm. ***B***, ***C***, Current-clamp recording of the simple spike firing of depolarized current-evoked PCs. ***B***, Representative traces of PCs simple spike firing evoked by a 300 pA depolarized current (duration, 500 ms) injected into the cells. Calibration: 25 mV, 100 ms. ***C***, Summary of PC spike firing frequency evoked by a series of depolarized currents injected to the cells from 0 to 600 pA in 100 pA increments (wild-type group: $n = 15$ cells from 3 mice; $CSMD3^{-/-}$ group: $n = 18$ cells from 3 mice; $CSMD3^{-/-}$ vs WT: $F_{(11,360)} = 2.98$; $p < 0.0001$). ***D***, ***E***, Current-clamp recording of spontaneous PC spike firing. ***D***, Representative traces of spontaneous PC spike firing in the wild-type and $CSMD3^{-/-}$ mice. Calibration: 20 mV, 100 ms. ***E***, Summary of the spontaneous PCs spike firing frequency (wild-type group: $n = 11$ cells from 6 mice; $CSMD3^{-/-}$ group: $n = 15$ cells from 3 mice; $CSMD3^{-/-}$ vs WT: $t_{(23)} = 0.10$, $p = 0.9199$). ***F***, Rheobase of PC spike firing evoked by a depolarized current injection in the wild-type and $CSMD3^{-/-}$ groups (wild-type group: $n = 15$ cells from 3 mice; $CSMD3^{-/-}$ group: $n = 18$ cells from 3 mice; $CSMD3^{-/-}$ vs WT: $t_{(31)} = 3.03$, $p = 0.0049$). ***G***, Schematic illustrating parameters reflecting the intrinsic membrane properties of PCs by an evoked AP. ***H***, Phase plots of PCs APs evoked by a series of depolarized currents injection in the wild-type and $CSMD3^{-/-}$ mice. ***I***, ***J***, Summary of threshold potential and action potential half-width in the wild-type and $CSMD3^{-/-}$ mice (wild-type group: $n = 15$ cells from 3 mice; $CSMD3^{-/-}$ group: 18 cells from 3 mice; $t_{(31)} = 5.95$, $p < 0.0001$ (***I***); $t_{(31)} = 2.50$, $p = 0.0181$ (***J***), $CSMD3^{-/-}$ vs WT). ***K***, ***L***, Summary graphs showing the ISI between the first and the second AP and the AP amplitude (wild-type group: $n = 15$ cells from 3 mice; $CSMD3^{-/-}$ group: $n = 18$ cells from 3 mice; $CSMD3^{-/-}$ vs WT: $t_{(31)} = 3.02$, $p = 0.005$ (***K***); $t_{(31)} = 1.33$, $p = 0.1923$ (***L***). ***M***, Representative traces illustrating the configuration for measuring the R_{in} of PCs. A hyperpolarizing current pulse (500 ms) in −50 pA was

vs *CSMD3*$^{-/-}$, 37.04 ± 4.77%; $p < 0.0001$, $F_{(1,16)} = 38.81$; Fig. 6*I–K*) in the cerebellum of *CSMD3*$^{-/-}$ mice when tasking from rest to run. In contrast, the calcium fluorescence was significantly decreased in both GABAergic cells ($n = 5$ mice/group; run: wild type, −17.60 ± 2.06%; vs *CSMD3*$^{-/-}$, 44.60 ± 3.08%; $p < 0.0001$; rest: wild type, −8.00 ± 1.61%; vs *CSMD3*$^{-/-}$, −3.00 ± 1.82%; $p = 0.5663$, $F_{(1,16)} = 166.80$; Fig. 6*F–H*) and PCs ($n = 5$ mice/group; run: wild type, 1.56 ± 0.74%; vs *CSMD3*$^{-/-}$, 34.99 ± 3.52%; $p < 0.0001$; rest: wild type, 0.86 ± 1.06%; vs *CSMD3*$^{-/-}$, 9.18 ± 1.63%; $p = 0.0634$, $F_{(1,16)} = 37.81$; Fig. 6*L–N*) in the cerebellum of *CSMD3*$^{-/-}$ mice when tasking from run to rest. However, the stimulation of movement had no significant influence on the calcium fluorescence signal intensity of both GABAergic cells and PCs in the wide-type mice when tasking either from rest to run (Fig. 6*C–E*, $p = 0.9986$; Fig. 6*I–K*, $p = 0.8145$) or from run to rest (Fig. 6*F–H*, $p = 0.0536$; Fig. 6*L–N*, $p > 0.9999$). These results suggest that loss of CSMD3 leads to increased neuronal activity of cerebellar PCs in response to movement activity.

CSMD3-deficient mice manifest aberrant increased excitability in cerebellar PCs

PCs are the sole output neurons of the cerebellar cortex and make inhibitory GABAergic synapses with their target neurons in the deep cerebellar nuclei (DCNs) and the vestibular nuclei (Hirano, 2018). PCs fire spontaneous APs even in the absence of synaptic inputs, and the PC firing rate is thought to be critical for encoding cerebellar output in DCNs (De Zeeuw et al., 2011). The intrinsic properties of PCs govern the functions of cerebellar circuits and have a major impact on its simple spike output (Zhou et al., 2014). We therefore examined the intrinsic excitability of PCs in the Crus I/II lobules by measuring their simple spikes using whole-cell patch-clamp recording in an acute mouse cerebellar slice (Fig. 7). Biocytin was added to the pipette solution, and validation of the recorded PCs was achieved by *post hoc* immunostaining of calbindin (the cerebellar PC marker) with biocytin (Fig. 7*A*). In addition, 3D reconstruction and Sholl analysis of biocytin-labeled PCs were conducted to examine the PCs morphology as mentioned previously in Figure 5. In line with the abnormal morphology and increased neuronal activity of PCs, a significant increase in the simple spike firing of PCs evoked by a series of depolarized currents (duration, 500 ms) injected into the cells from 0 to 600 pA in 100 pA increments, was found in the *CSMD3*$^{-/-}$ mice ($n = 15–18$ cells from 3 mice; $p < 0.0001$, $F_{(1,360)} = 2.98$; Fig. 7*B*,*C*). In contrast, there was no difference in spontaneous PC firing between the *CSMD3*$^{-/-}$ mice (38.00 ± 4.87 Hz) and the wild-type mice (37.09 ± 7.99 Hz; $n = 11–14$ cells from 3 mice; $p = 0.9199$, $t_{(23)} = 0.10$; Fig. 7*D*,*E*). In regard to intrinsic membrane properties, significant decreases in rheobase (wild type, 276.7 ± 27.97 pA; vs *CSMD3*$^{-/-}$, 177.8 ± 18.62 pA; $n = 15–18$ cells from 3 mice; $p = 0.0049$, $t_{(31)} = 3.03$; Fig. 7*F*) and threshold potential (wild type, −40.70 ± 0.75 mV; vs *CSMD3*$^{-/-}$, −46.21 ± 0.57 mV; $n = 15–18$ cells from 3 mice; $p < 0.0001$, $t_{(31)} = 5.95$; Fig. 7*H*,*I*), as well as in half-width of AP (wild type, 0.41 ± 0.01 ms; vs *CSMD3*$^{-/-}$, 0.37 ± 0.01 ms; $n = 15–18$ cells from 3 mice; $p = 0.0181$, $t_{(31)} = 2.50$; Fig. 7*J*) and interspike interval (ISI; wild type, 14.52 ± 2.15 ms; vs *CSMD3*$^{-/-}$, 7.88 ± 0.92 ms; $n = 15–18$ cells from 3 mice; $p = 0.0050$, $t_{(31)} = 3.02$; Fig. 7*K*) were observed in the PCs of *CSMD3*$^{-/-}$ mice compared with the wild-type mice. No significant difference was found in AP amplitude (wild type, 56.76 ± 2.05 mV; vs *CSMD3*$^{-/-}$, 60.40 ± 1.81 mV; $n = 15–18$ cells from 3 mice; $p = 0.1923$, $t_{(31)} = 1.33$; Fig. 7*L*) and R_{in} (wild type, 94.93 ± 4.39 MΩ; vs *CSMD3*$^{-/-}$, 118.0 ± 14.40 MΩ; $n = 15–18$ cells from 3 mice; $p = 0.1637$, $t_{(31)} = 1.41$; Fig. 7*M*,*N*) in the PCs between the two groups. Altogether, these data indicate that loss of CSMD3 causes enhanced intrinsic excitability of cerebellar PCs in the Crus I/II lobules, which may account for the increased neuronal activity of PCs in response to movement activity in the *CSMD3*$^{-/-}$ mice.

CSMD3-deficient mice display abnormal synaptic transmission and maladaptive synaptic plasticity in the cerebellum

PCs receive excitatory glutamatergic inputs from two distinct pathways: the mossy fiber–granule cell–PF–PC pathway that modulates the high-frequency "simple-spike" activity of PCs; and the CF–PC pathway arising in the inferior olive that creates infrequent calcium spikes, also called "complex spikes," in PCs (De Zeeuw et al., 2021). In addition, basket and stellate cells, collectively called "molecular layer interneurons" in the cerebellum, receive excitatory input from PF and inhibit PCs (De Zeeuw et al., 2021). In the cerebellum, fine-tuning of excitation–inhibition (E–I) balance plays an important role in cerebellar development and motor coordination (Sathyanesan et al., 2019). Alterations of any synaptic input to the PC leads to cerebellar symptoms (Hoxha et al., 2018). To determine whether loss of CSMD3 alters synaptic inputs to the PCs in the cerebellum, we investigate both mEPSC and mIPSC of PCs in the Crus I/II lobules using voltage-clamp recording in acute mouse cerebellar slices (Figs. 8*A–F*). The results showed that both amplitude (wild-type, 8.46 ± 0.27 pA; *CSMD3*–/–, 9.40 ± 0.21 pA) and frequency (wild-type, 1.96 ± 0.24 Hz; *CSMD3*–/–, 3.14 ± 0.30 Hz) of mEPSC of cerebellar PCs were significantly increased in the *CSMD3*$^{-/-}$ mice compared with wild-type mice ($n = 15–16$ cells from 4–5 mice/group; Fig. 8*B*: $p = 0.0114$, $t_{(29)} = 2.70$; Fig. 8*C*: $p = 0.0045$, $t_{(29)} = 3.08$). However, no significant difference was observed in mIPSC amplitude (wild type, 16.20 ± 1.84 pA; *CSMD3*$^{-/-}$, 20.43 ± 1.87 pA) and frequency (wild type, 10.91 ± 2.15 Hz; *CSMD3*$^{-/-}$, 15.71 ± 2.15 Hz) between the *CSMD3*$^{-/-}$ mice and the wild-type mice ($n = 15–16$ cells from 4 mice/group; Fig. 8*E*: $p = 0.1182$, $t_{(29)} = 1.61$; Fig. 8*F*: $p = 0.1253$, $t_{(29)} = 1.58$). These results indicate that loss of CSMD3 increases excitatory rather than inhibitory synaptic input to the PCs, thereby disrupting the E–I balance of synaptic transmission in the cerebellum.

In addition, synaptic plastic changes in the cerebellar circuit are thought to underlie motor learning and behavioral control, and LTD at PF–PC synapses has been considered to be a primary cellular mechanism for motor learning in the cerebellum (Hoxha et al., 2016). We thus proposed that loss of CSMD3 impairs LTD at the PF–PC synapses, which may underlie the dysfunction of the cerebellum and the pathology of ASD. As described in a previous study (Zhou et al., 2017), LTD of EPSCs at PF–PC synapses was examined by a conjunction of 5 PF pulses at 100 Hz and a 100 ms depolarization of PC to 0 mV, repeated 30 times with an interval of 2 s. The results showed that in the wild-type mice, a robust LTD at the PF–PC synapses in the Crus I/II lobules was elicited by this protocol; however, the same protocol was not able to induce significant LTD at the PF–PC synapses in the *CSMD3*$^{-/-}$ mice (Fig. 8*G–I*). When compared with the baseline

←

delivered to the cell to measure membrane R_{in}. ***N***, Summary graph showing the R_{in} of PCs in wild-type and *CSMD3*$^{-/-}$ mice ($n = 15–18$ cells from 3 mice/group; *CSMD3*$^{-/-}$ vs WT: $t_{(31)} = 1.41$, $p = 0.1637$). Data are presented as the mean ± SEM. *$p < 0.05$, **$p < 0.01$, ***$p < 0.001$, two-way ANOVA with Sidak's *post hoc* test (***C***); two-tailed unpaired *t* test for (***E***, ***F***, ***I***, ***J***, ***K***, ***L***, ***N***).

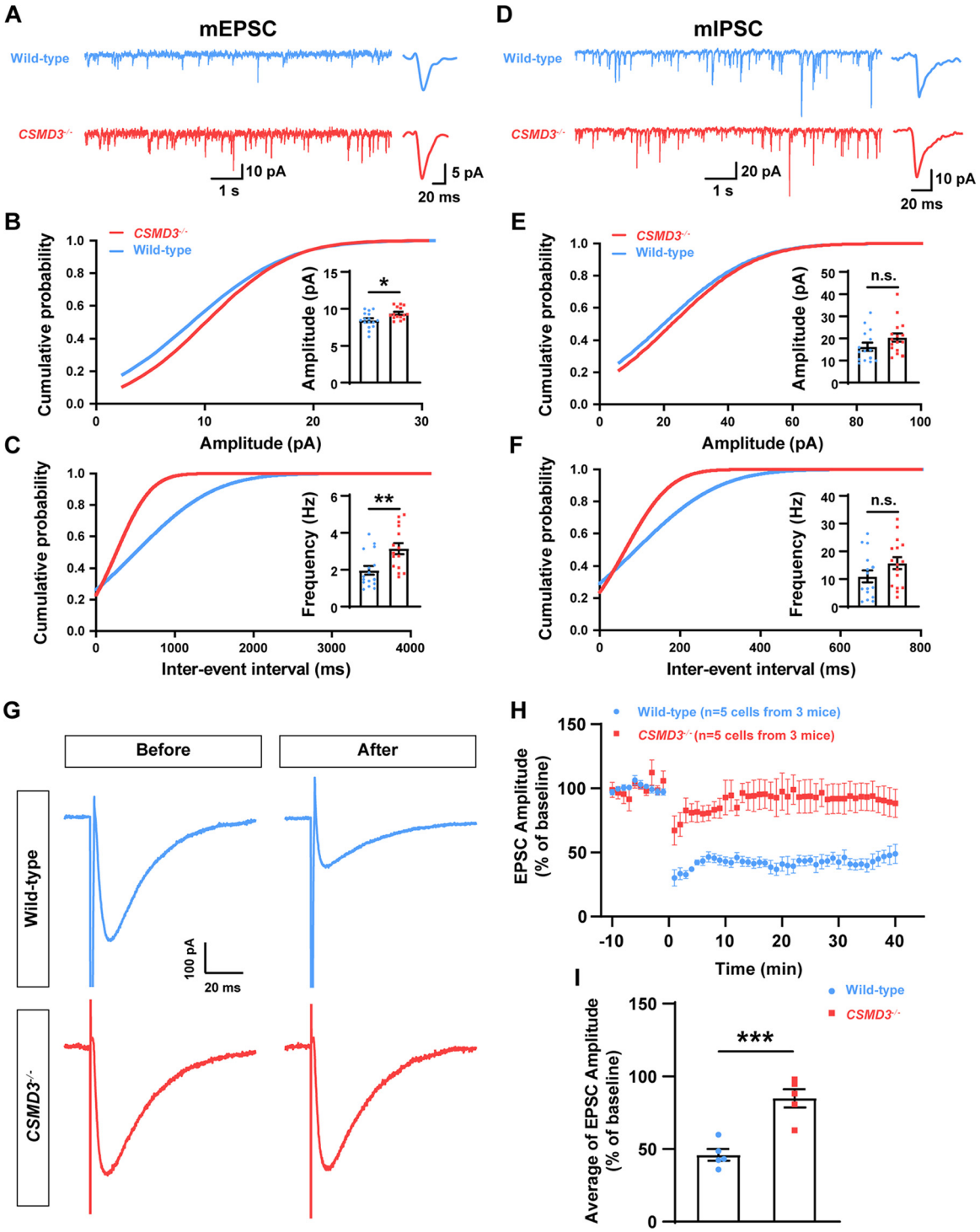

Figure 8. *CSMD3*-deficient mice display abnormal synaptic transmission and maladaptive synaptic plasticity in the cerebellum. ***A–C***, Whole-cell voltage-clamp recording of mEPSCs in cerebellar PCs. ***A***, Representative mEPSC traces in the wild-type (top) and *CSMD3*$^{-/-}$ (bottom) mice. Calibration: 10 pA, 1 s. Right, Examples of enlarged mEPSC trace. Calibration: 5 pA, 20 ms. ***B***, Cumulative distribution of mEPSC amplitude and plotted averaged amplitudes (inset bar graphs) from each recorded PC ($n = 16$ cells from 4–5 mice/group; $t_{(29)} = 2.70$, $p = 0.0114$). ***C***, Same as ***B***, but for instantaneous frequency of mEPSC ($n = 15$–16 cells from 4–5 mice/group; $t_{(29)} = 3.08$, $p = 0.0045$). ***D–F***, Whole-cell voltage-clamp recording of mIPSCs in cerebellar PCs. ***D***, Representative mIPSC traces in the wild-type (top) and *CSMD3*$^{-/-}$ (bottom) mice. Calibration: 20 pA, 1 s. Right, Examples of enlarged mIPSC trace. Calibration: 10 pA, 20 ms. ***E***, Cumulative distribution of mIPSC amplitude and plotted averaged amplitudes (inset bar graphs) from each recorded PC ($n = 15$–16 cells from 4 mice/group; $t_{(29)} = 1.61$, $p = 0.1182$). ***F***, Same as ***E***, but for mIPSC instantaneous frequency ($n = 15$–16 cells from 4 mice/group; $t_{(29)} = 1.58$, $p = 0.1253$). ***G–I***, LTD of EPSCs at PF–PC synapses recorded from the wild-type and *CSMD3*$^{-/-}$ mice. ***G***, ***H***, Representative traces of EPSC and the time course of changes in normalized EPSC amplitudes (percentage of baseline). ***G***, Representative traces of EPSC just before (left) and after (right) conjunctive stimulation in the wild-type (top) and *CSMD3*$^{-/-}$ (bottom) mice. Calibration: 100 pA, 20 ms. ***I***, Bar graph for the averaged EPSC amplitudes (normalized to baseline) during 40 min after conjunctive stimulation ($n = 5$ cells from 3–4 mice; $t_{(8)} = 5.24$, $p = 0.0008$). All EPSC amplitudes were normalized to baseline in percentiles. Data are presented as the mean ± SEM. $^{**}p < 0.01$, $^{***}p < 0.001$; n.s., no statistical difference, compared between the wild-type and *CSMD3*$^{-/-}$ groups; two-tailed unpaired *t* test (***B***, ***C***, ***E***, ***F***, ***I***).

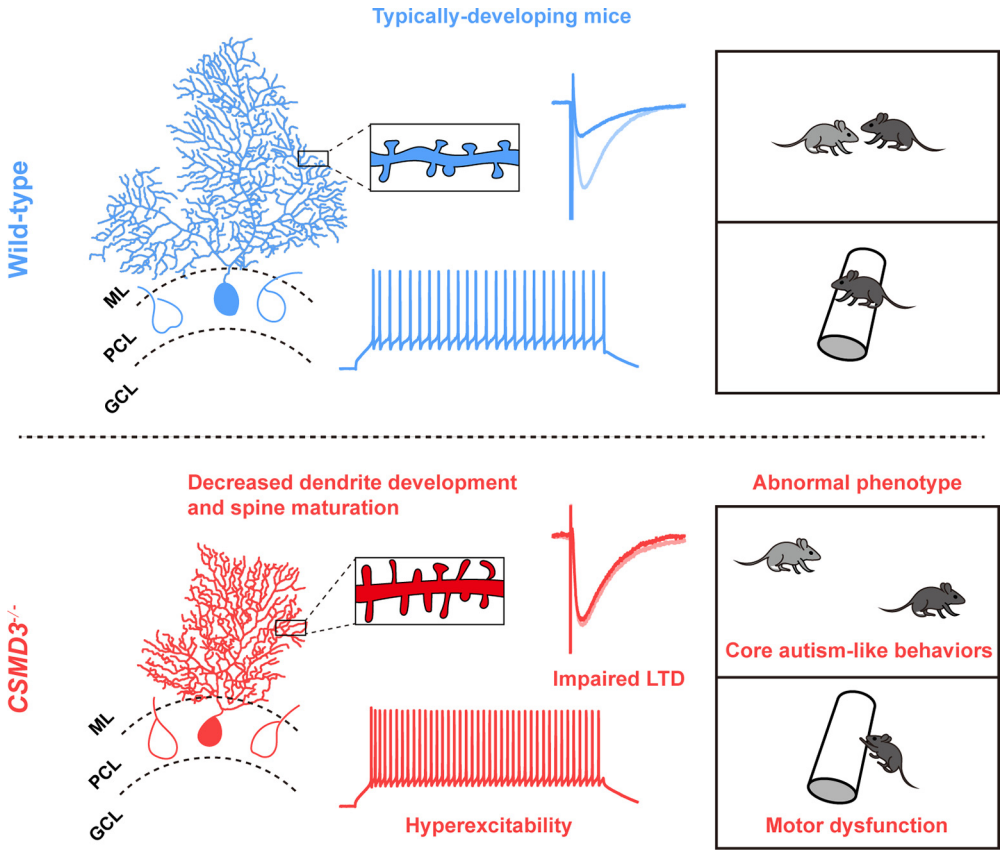

Figure 9. Schematic summary of proposed pathologic changes underlying cerebellar motor dysfunction and autism-like behaviors in CSMD3-deficient mice. CSMD3 deficiency leads to abnormally decreased dendritic complexity but increased immature spine density of cerebellar PCs. Moreover, intrinsic excitability of cerebellar PCs is dramatically increased, and LTD at PF–PC synapses is impaired in the cerebellum of *CSMD3*$^{-/-}$ mice. These data suggest that the loss of CSMD3 results in abnormal morphology, increased intrinsic excitabilities, and impaired synaptic plasticity in cerebellar PCs, subsequently leading to motor deficits and autism-like behaviors in mice. GCL, Granular cell layer.

responses (averaged at 0–10 min before stimulation), the mean EPSC amplitude after stimulation was increased from 45.98 ± 4.01% of the wild-type group to 84.89 ± 6.25% of the *CSMD3*$^{-/-}$ group ($n = 5$ mice/group; $p = 0.0008$, $t_{(8)} = 5.24$; Fig. 8*I*). Together, these data suggest that loss of CSMD3 leads to increased excitatory synaptic input to the PC and impaired LTD at the PF–PC synapses, subsequently destroys E–I balance in synaptic transmission, and causes maladaptive synaptic plasticity in the cerebellum, which are probably implicated in motor deficits and ASD pathology because of cerebellar dysfunction.

Discussion

In this study, we demonstrate for the first time, to our knowledge, that loss of CSMD3 results in abnormal morphology and dysfunction of cerebellar Crus I/II PCs, which are highly correlated to motor deficits and cognitive function impairments as manifested in ASD (Fatemi et al., 2012). *CSMD3* is a giant gene expressed mainly in fetal and adult brains (Shimizu et al., 2003). Here we found that the CSMD3 is highly expressed in neurons and oligodendrocytes, located at the cerebellum, hippocampus, and other regions in the brain. CSMD3 may act as a coreceptor of an unidentified membrane protein to regulate dendrite development in cultured hippocampal neurons (Mizukami et al., 2016), we thus suggest that malfunctions of CSMD3 may impair neuronal development and maturation, and may cause abnormal cerebellar dysfunction, thereby resulting in the pathology of ASD (van der Heijden et al., 2021). Indeed, mutations of the *CSMD3* gene have been found in two patients with ASD (Floris et al., 2008), and genetic deletion of *CSMD3* caused core autistic-like symptoms and motor dysfunction in mice, further supporting the conception that the *CSMD3* gene may be a candidate for ASD (Floris et al., 2008). Using whole-genome sequencing screen, Wu et al. (2018) identified six damaged nonsynonymous mutations in *CSMD3* gene in 3 of 32 patients with ASD in the People's Republic of China. Intronic deletion of *CSMD3* gene was detected in subjects with a diagnosis of trios of ASD, schizophrenia, and bipolar disorder (Malhotra et al., 2011), indicating that the contribution of *CSMD3* mutations to the onset of ASD are specific and rare.

We observed that motor and nonmotor behaviors are strongly affected in *CSMD3*-deficient mice. It raises a possibility that the reduced sociability and social novelty is probably caused by the altered locomotor activity in *CSMD3*-mutant mice. To clarify this question, we performed a three-chamber social test to evaluate the sociability and social novelty as well as the locomotor activity of mice. We found that in contrast to the reduction of social preference index and social novelty index, the number of entries in each chamber was not affected, indicating normal exploration activity in *CSMD3*-deficient mice (Carta et al., 2019). These findings may exclude the possibility that the reduced sociability and social novelty are caused by the altered locomotor activity in *CSMD3*-mutant mice. Additional control experiments, including spontaneous digging time and NOR test were performed to determine the potential causes for the phenotype observed in the marble-burying test. The normal spontaneous

digging time may indicate the unimpaired innate behaviors, whereas the decreased recognition index illustrates a decreased novelty-seeking activity in *CSMD3*-deficient mice. Together, these findings with the decreased exploring time observed in EPM test, we speculate that the reduced marble burying observed in *CSMD3*-deficient mice is probably the result of a lack of novelty-seeking behavior rather than a direct consequence of altered locomotion or an impairment of innate behaviors such as digging. In addition, anxiety is a frequent symptom associated with ASD patients (van Steensel et al., 2011). OFT and EPM test were applied to measure anxiety-like behaviors in *CSMD3*-mutant mice. Although the time spent in the center was not reduced in *CSMD3*-mutant mice observed in the OFT, both the decreased time exploring the open arms and the reduced number of entries into the open arms, as tested in the EPM test, indicated anxiety-like behaviors in *CSMD3*-mutant mice.

Although motor deficits are not classically considered a core symptom of ASD, a high proportion of ASD patients display motor performance and motor learning abnormalities (Rinehart et al., 2006; Kindregan et al., 2015). Difficulties with motor coordination and learning, seen in both patients and mice, point to an involvement of the cerebellum in ASD pathology (Mapelli et al., 2022). Because motor impairments provide an alternative, scientifically rigorous approach to understanding ASD symptoms, the cerebellar-driven motor behaviors thereby are suited to complement social behavior studies for the identification of molecular and cellular causes of ASD phenotypes (Simmons et al., 2021). Cerebellar abnormalities, particularly in Crus I/II lobules, are consistently reported in ASD patients (D'Mello and Stoodley, 2015; Guell et al., 2018). In preclinical studies, PC dopamine D_2 receptor levels in Crus I/II lobules are reported to regulate social behaviors (Cutando et al., 2022), and disrupted Right Crus I-cerebral cortical connectivity is evident in the PC *Tsc1*-mutant ASD mouse model (Stoodley et al., 2017), indicating the importance of Crus I/II lobules in the control of social behaviors and their altered functions in ASD. Moreover, morphologic and functional changes in the cerebellum are reported in various neurodevelopmental disorders including ASD (Sydnor and Aldinger, 2022). Consistently, we observed abnormal cerebellar PC morphology in Crus I/II lobules, including reduced dendritic arborization and total dendrite length, and increased spine density and length, but decreased spine head width in *CSMD3*$^{-/-}$ mice. It is well documented that PCs bear large numbers of spines (Nimchinsky et al., 2002), and spine density is known to decrease as PC maturation proceeds (McKay and Turner, 2005). Therefore, our observations of enhanced spine density in the knockouts probably indicate a general underdevelopment of PC spinogenesis. Except for density, morphologies of dendritic spines are also thought to underlie synaptic strength (Borczyk et al., 2019). Several lines of evidence suggest that long and thin spines without bulbous heads, like filopodia, play a pivotal role in the initial stages of spinogenesis (Nimchinsky et al., 2002; Bhatt et al., 2009). Because of the high density of spines, it is difficult to recognize different spine subtypes accurately on PC dendrites; hence, we performed sparse labeling of PCs to measure spine length and head width (Sugawara et al., 2017). The increased length but the decreased head width observed in PC dendritic spines indicate that a much greater proportion of immature spines existed in *CSMD3*$^{-/-}$ mice.

In addition to these abnormal alterations of cerebellar PCs morphology, an increased neuronal activity of Crus I/II PCs was found in response to movement activity in *CSMD3*$^{-/-}$ mice. The increased and decreased calcium fluorescence signals of both GABAergic cells and PCs, which, respectively, are relevant to tasking from rest to run and run to rest, indicate an aberrant neuronal activity of Crus I/II PCs, which may account for the motor dysfunction displayed in *CSMD3*$^{-/-}$ mice. Consistently, previous studies revealed that in typically developing individuals, activation of cerebellar Crus I/II lobules is found during some "nonmotor" tasks (Stoodley et al., 2010, 2012), but not during simple motor tasks (Desmond et al., 1997). Abnormal activation of Crus I/II PCs may reflect the abnormal functional circuitry between the nonmotor and motor areas that has been reported in ASD (Khan et al., 2015).

In addition, alterations in the generation of PC action potentials are considered responsible for cerebellar motor deficits and, as well, for ASD-related symptoms (Tsai et al., 2012). Here we found an enhanced intrinsic excitability of Crus I/II PCs and increased excitatory input from PFs, which modulate the high-frequency simple-spike activity of PCs (De Zeeuw et al., 2021). Also, we observed a significant increase in the amplitude and frequency of mEPSCs, but not mIPSCs, in Crus I/II PCs in *CSMD3*$^{-/-}$ mice, suggesting an increase of excitatory rather than inhibitory synaptic input to Crus I/II PCs. In the cerebellum, fine-tuning of E–I balance plays an important role in cerebellar development and motor coordination (Sathyanesan et al., 2019). Alterations of any synaptic input to the PC leads to cerebellar symptoms (Hoxha et al., 2018). We thus hypothesized that this E–I imbalance of synaptic transmission in the cerebellum likely results in cerebellar symptoms, which are manifested in the ASD.

Apart from aberrant intrinsic excitability of PCs and E–I imbalance of synaptic transmission in the cerebellum, we also found an impaired LTD at the PF–PC synapse in Crus I/II lobules of the *CSMD3*$^{-/-}$ mice. It has previously been pointed out that the molecular machinery for spine/synapse pruning is almost identical to that for LTD (in particular in the cerebellum; Piochon et al., 2016). Our observations of enhanced spine density as well as the increased proportion of immature spines indicate an impaired spine/synapse pruning exhibited in Crus I/II PCs, which may in part account for the impaired cerebellar LTD observed in *CSMD3*$^{-/-}$ mice. LTD is considered to be a cellular mechanism underlying motor learning (Ito et al., 2014), and impaired LTD prevents proper motor learning in cerebellum-dependent tasks (Alba et al., 1994; De Zeeuw et al., 1998). The contribution of movements to social cognition and cascade effects on social communication in individuals with autism have been reported (Cook, 2016; Baranek et al., 2018), thereby raising a possibility that motor disturbances, caused by impaired cerebellar LTD, may underlie some of the behavioral core features in autism.

In conclusion, this study demonstrates that CSMD3 plays an important role in cerebellar PCs development. Loss of CSMD3 results in abnormal PC morphology and dysfunction in cerebellar Crus I/II lobules, which may underlie the pathogenesis of motor deficits and core autistic-like symptoms in *CSMD3*$^{-/-}$ mice (Fig. 9). These results provide novel insight into the pathophysiological mechanisms by which *CSMD3* mutations cause impairments of cerebellar function that may contribute to ASD.

References

Alba A, Kano M, Chen C, Stanton ME, Fox GD, Herrup K, Zwingman TA, Tonegawa S (1994) Deficient cerebellar long-term depression and impaired motor learning in mGluR1 mutant mice. Cell 79:377–388.

Amaral DG, Schumann CM, Nordahl CW (2008) Neuroanatomy of autism. Trends Neurosci 31:137–145.

Baranek GT, Woynaroski TG, Nowell S, Turner-Brown L, DuBay M, Crais ER, Watson LR (2018) Cascading effects of attention disengagement and sensory seeking on social symptoms in a community sample of infants at-risk for a future diagnosis of autism spectrum disorder. Dev Cogn Neurosci 29:30–40.

Bauman ML, Kemper TL (2005) Neuroanatomic observations of the brain in autism: a review and future directions. Int J Dev Neurosci 23:183–187.

Bhatt DH, Zhang S, Gan WB (2009) Dendritic spine dynamics. Annu Rev Physiol 71:261–282.

Borczyk M, Śliwińska MA, Caly A, Bernas T, Radwanska K (2019) Neuronal plasticity affects correlation between the size of dendritic spine and its postsynaptic density. Sci Rep 9:1693.

Carta I, Chen CH, Schott AL, Dorizan S, Khodakhah K (2019) Cerebellar modulation of the reward circuitry and social behavior. Science 363:

Chao OY, de Souza Silva MA, Yang YM, Huston JP (2020) The medial prefrontal cortex - hippocampus circuit that integrates information of object, place and time to construct episodic memory in rodents: behavioral, anatomical and neurochemical properties. Neurosci Biobehav Rev 113: 373–407.

Chen G, Sima J, Jin M, Wang KY, Xue XJ, Zheng W, Ding YQ, Yuan XB (2008) Semaphorin-3A guides radial migration of cortical neurons during development. Nat Neurosci 11:36–44.

Cook J (2016) From movement kinematics to social cognition: the case of autism. Philos Trans R Soc Lond B Biol Sci 371:20150372.

Courtney CD, Christian CA (2018) Subregion-specific impacts of genetic loss of diazepam binding inhibitor on synaptic inhibition in the murine hippocampus. Neuroscience 388:128–138.

Crawley JN (2007) Mouse behavioral assays relevant to the symptoms of autism. Brain Pathol 17:448–459.

Cruz-Sanchez A, Dematagoda S, Ahmed R, Mohanathaas S, Odenwald N, Arruda-Carvalho M (2020) Developmental onset distinguishes three types of spontaneous recognition memory in mice. Sci Rep 10:10612.

Cupolillo D, Hoxha E, Faralli A, De Luca A, Rossi F, Tempia F, Carulli D (2016) Autistic-like traits and cerebellar dysfunction in Purkinje cell PTEN knock-out mice. Neuropsychopharmacology 41:1457–1466.

Cutando L, Puighermanal E, Castell L, Tarot P, Belle M, Bertaso F, Arango-Lievano M, Ango F, Rubinstein M, Quintana A, Chédotal A, Mameli M, Valjent E (2022) Cerebellar dopamine D2 receptors regulate social behaviors. Nat Neurosci 25:900–911.

D'Mello AM, Stoodley CJ (2015) Cerebro-cerebellar circuits in autism spectrum disorder. Front Neurosci 9:408.

Damseh N, et al. (2015) Mutations in SLC1A4, encoding the brain serine transporter, are associated with developmental delay, microcephaly and hypomyelination. J Med Genet 52:541–547.

Deng S, Li J, He Q, Zhang X, Zhu J, Li L, Mi Z, Yang X, Jiang M, Dong Q, Mao Y, Shu Y (2020) Regulation of recurrent inhibition by asynchronous glutamate release in neocortex. Neuron 105:522–533.e4.

Desmond JE, Gabrieli JD, Wagner AD, Ginier BL, Glover GH (1997) Lobular patterns of cerebellar activation in verbal working-memory and finger-tapping tasks as revealed by functional MRI. J Neurosci 17:9675–9685.

De Zeeuw CI, Hansel C, Bian F, Koekkoek SK, van Alphen AM, Linden DJ, Oberdick J (1998) Expression of a protein kinase C inhibitor in Purkinje cells blocks cerebellar LTD and adaptation of the vestibulo-ocular reflex. Neuron 20:495–508.

De Zeeuw CI, Hoebeek FE, Bosman LW, Schonewille M, Witter L, Koekkoek SK (2011) Spatiotemporal firing patterns in the cerebellum. Nat Rev Neurosci 12:327–344.

De Zeeuw CI, Lisberger SG, Raymond JL (2021) Diversity and dynamism in the cerebellum. Nat Neurosci 24:160–167.

Fang D, Kong LY, Cai J, Li S, Liu XD, Han JS, Xing GG (2015) Interleukin-6-mediated functional upregulation of TRPV1 receptors in dorsal root ganglion neurons through the activation of JAK/PI3K signaling pathway: roles in the development of bone cancer pain in a rat model. Pain 156:1124–1144.

Fatemi SH, et al. (2012) Consensus paper: pathological role of the cerebellum in autism. Cerebellum 11:777–807.

Floris C, Rassu S, Boccone L, Gasperini D, Cao A, Crisponi L (2008) Two patients with balanced translocations and autistic disorder: CSMD3 as a candidate gene for autism found in their common 8q23 breakpoint area. Eur J Hum Genet 16:696–704.

Fournier KA, Hass CJ, Naik SK, Lodha N, Cauraugh JH (2010) Motor coordination in autism spectrum disorders: a synthesis and meta-analysis. J Autism Dev Disord 40:1227–1240.

Gaboriaud C, Gregory-Pauron L, Teillet F, Thielens NM, Bally I, Arlaud GJ (2011) Structure and properties of the Ca(2+)-binding CUB domain, a widespread ligand-recognition unit involved in major biological functions. Biochem J 439:185–193.

Gilbert J, O'Connor M, Templet S, Moghaddam M, Di Via Ioschpe A, Sinclair A, Zhu LQ, Xu W, Man HY (2020) NEXMIF/KIDLIA knock-out mouse demonstrates autism-like behaviors, memory deficits, and impairments in synapse formation and function. J Neurosci 40:237–254.

Greco B, Managò F, Tucci V, Kao HT, Valtorta F, Benfenati F (2013) Autism-related behavioral abnormalities in synapsin knockout mice. Behav Brain Res 251:65–74.

Green D, Charman T, Pickles A, Chandler S, Loucas T, Simonoff E, Baird G (2009) Impairment in movement skills of children with autistic spectrum disorders. Dev Med Child Neurol 51:311–316.

Guell X, Schmahmann JD, Gabrieli J, Ghosh SS (2018) Functional gradients of the cerebellum. Elife 7:e36652.

Gunnersen JM, Kim MH, Fuller SJ, De Silva M, Britto JM, Hammond VE, Davies PJ, Petrou S, Faber ES, Sah P, Tan SS (2007) Sez-6 proteins affect dendritic arborization patterns and excitability of cortical pyramidal neurons. Neuron 56:621–639.

Guo B, Chen J, Chen Q, Ren K, Feng D, Mao H, Yao H, Yang J, Liu H, Liu Y, Jia F, Qi C, Lynn-Jones T, Hu H, Fu Z, Feng G, Wang W, Wu S (2019) Anterior cingulate cortex dysfunction underlies social deficits in Shank3 mutant mice. Nat Neurosci 22:1223–1234.

Hampson DR, Blatt GJ (2015) Autism spectrum disorders and neuropathology of the cerebellum. Front Neurosci 9:420.

Hanaie R, Mohri I, Kagitani-Shimono K, Tachibana M, Matsuzaki J, Hirata I, Nagatani F, Watanabe Y, Katayama T, Taniike M (2018) Aberrant cerebellar-cerebral functional connectivity in children and adolescents with autism spectrum disorder. Front Hum Neurosci 12:454.

Harris SR (2017) Early motor delays as diagnostic clues in autism spectrum disorder. Eur J Pediatr 176:1259–1262.

Havdahl A, Niarchou M, Starnawska A, Uddin M, van der Merwe C, Warrier V (2021) Genetic contributions to autism spectrum disorder. Psychol Med 51:2260–2273.

Hirano T (2018) Purkinje neurons: development, morphology, and function. Cerebellum 17:699–700.

Hoxha E, Tempia F, Lippiello P, Miniaci MC (2016) Modulation, plasticity and pathophysiology of the parallel fiber-Purkinje cell synapse. Front Synaptic Neurosci 8:35.

Hoxha E, Balbo I, Miniaci MC, Tempia F (2018) Purkinje cell signaling deficits in animal models of ataxia. Front Synaptic Neurosci 10:6.

Huang S, Zheng C, Xie G, Song Z, Wang P, Bai Y, Chen D, Zhang Y, Lv P, Liang W, She S, Li Q, Liu Z, Wang Y, Xing GG, Wang Y (2021) FAM19A5/TAFA5, a novel neurokine, plays a crucial role in depressive-like and spatial memory-related behaviors in mice. Mol Psychiatry 26:2363–2379.

Ito M, Yamaguchi K, Nagao S, Yamazaki T (2014) Long-term depression as a model of cerebellar plasticity. Prog Brain Res 210:1–30.

Kaplan E, Zubedat S, Radzishevsky I, Wolosker H (2018) ASCT1 (Slc1a4) transporter is a physiologic regulator of brain D-serine and neurodevelopment. Proc Natl Acad Sci U S A 115:9628–9633.

Khan AJ, Nair A, Keown CL, Datko MC, Lincoln AJ, Müller RA (2015) Cerebro-cerebellar resting-state functional connectivity in children and adolescents with autism spectrum disorder. Biol Psychiatry 78:625–634.

Kindregan D, Gallagher L, Gormley J (2015) Gait deviations in children with autism spectrum disorders: a review. Autism Res Treat 2015:741480.

Lau WL, Scholnick SB (2003) Identification of two new members of the CSMD gene family. Genomics 82:412–415.
Liang YJ, Feng SY, Qi YP, Li K, Jin ZR, Jing HB, Liu LY, Cai J, Xing GG, Fu KY (2019) Contribution of microglial reaction to increased nociceptive responses in high-fat-diet (HFD)-induced obesity in male mice. Brain Behav Immun 80:777–792.
Limperopoulos C, Bassan H, Gauvreau K, Robertson RL Jr, Sullivan NR, Benson CB, Avery L, Stewart J, Soul JS, Ringer SA, Volpe JJ, duPlessis AJ (2007) Does cerebellar injury in premature infants contribute to the high prevalence of long-term cognitive, learning, and behavioral disability in survivors? Pediatrics 120:584–593.
Lord C, Elsabbagh M, Baird G, Veenstra-Vanderweele J (2018) Autism spectrum disorder. Lancet 392:508–520.
Malhotra D, et al. (2011) High frequencies of de novo CNVs in bipolar disorder and schizophrenia. Neuron 72:951–963.
Mapelli L, Soda T, D'Angelo E, Prestori F (2022) The cerebellar involvement in autism spectrum disorders: from the social brain to mouse models. Int J Mol Sci 23:3894.
McKay BE, Turner RW (2005) Physiological and morphological development of the rat cerebellar Purkinje cell. J Physiol 567:829–850.
McLaurin J, Trudel GC, Shaw IT, Antel JP, Cashman NR (1995) A human glial hybrid cell line differentially expressing genes subserving oligodendrocyte and astrocyte phenotype. J Neurobiol 26:283–293.
Menashe I, Grange P, Larsen EC, Banerjee-Basu S, Mitra PP (2013) Co-expression profiling of autism genes in the mouse brain. PLoS Comput Biol 9:e1003128.
Mizukami T, Kohno T, Hattori M (2016) CUB and Sushi multiple domains 3 regulates dendrite development. Neurosci Res 110:11–17.
Moy SS, Nadler JJ, Young NB, Nonneman RJ, Grossman AW, Murphy DL, D'Ercole AJ, Crawley JN, Magnuson TR, Lauder JM (2009) Social approach in genetically engineered mouse lines relevant to autism. Genes Brain Behav 8:129–142.
Nimchinsky EA, Sabatini BL, Svoboda K (2002) Structure and function of dendritic spines. Annu Rev Physiol 64:313–353.
Oeschger FM, Wang W-Z, Lee S, García-Moreno F, Goffinet AM, Arbonés ML, Rakic S, Molnár Z (2012) Gene expression analysis of the embryonic subplate. Cereb Cortex 22:1343–1359.
Oldehinkel M, et al. (2019) Altered connectivity between cerebellum, visual, and sensory-motor networks in autism spectrum disorder: results from the EU-AIMS Longitudinal European Autism Project. Biol Psychiatry Cogn Neurosci Neuroimaging 4:260–270.
Oristaglio J, Hyman West S, Ghaffari M, Lech MS, Verma BR, Harvey JA, Welsh JP, Malone RP (2013) Children with autism spectrum disorders show abnormal conditioned response timing on delay, but not trace, eyeblink conditioning. Neuroscience 248:708–718.
Peça J, Feliciano C, Ting JT, Wang W, Wells MF, Venkatraman TN, Lascola CD, Fu Z, Feng G (2011) Shank3 mutant mice display autistic-like behaviours and striatal dysfunction. Nature 472:437–442.
Peter S, Ten Brinke MM, Stedehouder J, Reinelt CM, Wu B, Zhou H, Zhou K, Boele HJ, Kushner SA, Lee MG, Schmeisser MJ, Boeckers TM, Schonewille M, Hoebeek FE, De Zeeuw CI (2016) Dysfunctional cerebellar Purkinje cells contribute to autism-like behaviour in Shank2-deficient mice. Nat Commun 7:12627.
Piochon C, Kloth AD, Grasselli G, Titley HK, Nakayama H, Hashimoto K, Wan V, Simmons DH, Eissa T, Nakatani J, Cherskov A, Miyazaki T, Watanabe M, Takumi T, Kano M, Wang SS, Hansel C (2014) Cerebellar plasticity and motor learning deficits in a copy-number variation mouse model of autism. Nat Commun 5:5586.
Piochon C, Kano M, Hansel C (2016) LTD-like molecular pathways in developmental synaptic pruning. Nat Neurosci 19:1299–1310.
Qi X, Cui K, Zhang Y, Wang L, Tong J, Sun W, Shao S, Wang J, Wang C, Sun X, Xiao L, Xi K, Cui S, Liu F, Ma L, Zheng J, Yi M, Wan Y (2022) A nociceptive neuronal ensemble in the dorsomedial prefrontal cortex underlies pain chronicity. Cell Rep 41:111833.
Ramos TC, Balardin JB, Sato JR, Fujita A (2019) Abnormal cortico-cerebellar functional connectivity in autism spectrum disorder. Front Syst Neurosci 12:74.
Rinehart NJ, Tonge BJ, Iansek R, McGinley J, Brereton AV, Enticott PG, Bradshaw JL (2006) Gait function in newly diagnosed children with autism: cerebellar and basal ganglia related motor disorder. Dev Med Child Neurol 48:819–824.
Sathyanesan A, Zhou J, Scafidi J, Heck DH, Sillitoe RV, Gallo V (2019) Emerging connections between cerebellar development, behaviour and complex brain disorders. Nat Rev Neurosci 20:298–313.
Shimizu A, Asakawa S, Sasaki T, Yamazaki S, Yamagata H, Kudoh J, Minoshima S, Kondo I, Shimizu N (2003) A novel giant gene CSMD3 encoding a protein with CUB and sushi multiple domains: a candidate gene for benign adult familial myoclonic epilepsy on human chromosome 8q23.3–q24.1. Biochem Biophys Res Commun 309:143–154.
Shimoda S, Ozawa T, Ichitani Y, Yamada K (2021) Long-term associative memory in rats: effects of familiarization period in object-place-context recognition test. PLoS One 16:e0254570.
Sia GM, Clem RL, Huganir RL (2013) The human language-associated gene SRPX2 regulates synapse formation and vocalization in mice. Science 342:987–991.
Simmons DH, Titley HK, Hansel C, Mason P (2021) Behavioral tests for mouse models of autism: an argument for the inclusion of cerebellum-controlled motor behaviors. Neuroscience 462:303–319.
Skefos J, Cummings C, Enzer K, Holiday J, Weed K, Levy E, Yuce T, Kemper T, Bauman M (2014) Regional alterations in Purkinje cell density in patients with autism. PLoS One 9:e81255.
Stoodley CJ (2014) Distinct regions of the cerebellum show gray matter decreases in autism, ADHD, and developmental dyslexia. Front Syst Neurosci 8:92.
Stoodley CJ, Valera EM, Schmahmann JD (2010) An fMRI study of intra-individual functional topography in the human cerebellum. Behav Neurol 23:65–79.
Stoodley CJ, Valera EM, Schmahmann JD (2012) Functional topography of the cerebellum for motor and cognitive tasks: an fMRI study. Neuroimage 59:1560–1570.
Stoodley CJ, D'Mello AM, Ellegood J, Jakkamsetti V, Liu P, Nebel MB, Gibson JM, Kelly E, Meng F, Cano CA, Pascual JM, Mostofsky SH, Lerch JP, Tsai PT (2017) Altered cerebellar connectivity in autism and cerebellar-mediated rescue of autism-related behaviors in mice. Nat Neurosci 20:1744–1751.
Su LD, Xu FX, Wang XT, Cai XY, Shen Y (2021) Cerebellar dysfunction, cerebro-cerebellar connectivity and autism spectrum disorders. Neuroscience 462:320–327.
Sugawara T, Hisatsune C, Miyamoto H, Ogawa N, Mikoshiba K (2017) Regulation of spinogenesis in mature Purkinje cells via mGluR/PKC-mediated phosphorylation of CaMKIIbeta. Proc Natl Acad Sci U S A 114:E5256–E5265.
Suliman-Lavie R, Title B, Cohen Y, Hamada N, Tal M, Tal N, Mondereer-Rothkoff G, Gudmundsdottir B, Gudmundsson KO, Keller JR, Huang GJ, Nagata KI, Yarom Y, Shifman S (2020) Pogz deficiency leads to transcription dysregulation and impaired cerebellar activity underlying autism-like behavior in mice. Nat Commun 11:5836.
Sydnor LM, Aldinger KA (2022) Structure, function, and genetics of the cerebellum in autism. J Psychiatr Brain Sci 7:e220008.
Thomas A, Burant A, Bui N, Graham D, Yuva-Paylor LA, Paylor R (2009) Marble burying reflects a repetitive and perseverative behavior more than novelty-induced anxiety. Psychopharmacology (Berl) 204:361–373.
Tsai PT, Hull C, Chu Y, Greene-Colozzi E, Sadowski AR, Leech JM, Steinberg J, Crawley JN, Regehr WG, Sahin M (2012) Autistic-like behaviour and cerebellar dysfunction in Purkinje cell Tsc1 mutant mice. Nature 488:647–651.
van der Heijden ME, Gill JS, Sillitoe RV (2021) Abnormal cerebellar development in autism spectrum disorders. Dev Neurosci 43:181–190.
van Steensel FJ, Bögels SM, Perrin S (2011) Anxiety disorders in children and adolescents with autistic spectrum disorders: a meta-analysis. Clin Child Fam Psychol Rev 14:302–317.
Wang Y, Zeng C, Li J, Zhou Z, Ju X, Xia S, Li Y, Liu A, Teng H, Zhang K, Shi L, Bi C, Xie W, He X, Jia Z, Jiang Y, Cai T, Wu J, Xia K, Sun ZS (2018) PAK2 haploinsufficiency results in synaptic cytoskeleton impairment and autism-related behavior. Cell Rep 24:2029–2041.
Wilson RB, Enticott PG, Rinehart NJ (2018) Motor development and delay: advances in assessment of motor skills in autism spectrum disorders. Curr Opin Neurol 31:134–139.

Wu J, et al. (2018) Genomic landscapes of Chinese sporadic autism spectrum disorders revealed by whole-genome sequencing. J Genet Genomics 45:527–538.

Zhao JJ, Hu JX, Lu DX, Ji CX, Qi Y, Liu XY, Sun FY, Huang F, Xu P, Chen XH (2017) Soluble cpg15 from astrocytes ameliorates neurite outgrowth recovery of hippocampal neurons after mouse cerebral ischemia. J Neurosci 37:1628–1647.

Zhou H, Lin Z, Voges K, Ju C, Gao Z, Bosman LW, Ruigrok TJ, Hoebeek FE, De Zeeuw CI, Schonewille M (2014) Cerebellar modules operate at different frequencies. Elife 3:e02536.

Zhou JH, Wang XT, Zhou L, Zhou L, Xu FX, Su LD, Wang H, Jia F, Xu FQ, Chen GQ, De Zeeuw CI, Shen Y (2017) Ablation of TFR1 in Purkinje cells inhibits mGlu1 trafficking and impairs motor coordination, but not autistic-like behaviors. J Neurosci 37:11335–11352.